Case History

Gravimetry and petrophysics for defining the intracratonic and rift basins of the Western-Central Africa zone

Francesca Maddaloni[1], Tommaso Pivetta[1], and Carla Braitenberg[1]

ABSTRACT

The global gravity field obtained from the observations of the satellite Gravity Field and Steady-State Ocean Circulation Explorer (GOCE) satellite offers new opportunities in defining density variations of earth's crust and mantle, allowing new insights into the structure of specific geologic features. The Central African Rift is a key feature in understanding the dismemberment of Gondwana, and we contribute to defining the crustal density structure underlying the rift. The presence of a narrow and up to 12 km deep basin implies crustal stretching allowed the sediment to accumulate, but a key question is whether the stretching processes also affected the deeper layers of the crust or was limited to the upper crust. The study area includes a subbasin of the greater Chad sag basin, which extends over 1500 × 1500 km and occupies the center of North-Central Africa, shared between the countries of Chad, Sudan, Nigeria, Niger, Algeria, Libya, and Cameroon. We find that the rifting affected the lower crust of the West African Rift, and we evaluate evidence for a 1500 km long and several km thick magmatic crustal intrusion presumably associated with underplating and crustal thinning. We estimate that the stretching factor must be at least 1.5 and had affected the entire crust. To our knowledge, the identification of a continuous body of magmatic intrusions is new and has been only possible through the recent global gravity field. The magmatism has altered the thermal conditions from the time of emplacement on, and it is relevant for the maturation of hydrocarbons present in the sediments. The timing of the magmatism is presumably tied to two pulses of volcanism documented in the rift, associated with the first postrift phase from 96 to 88 Ma and the second postrift phase from 23 Ma up to the Quaternary.

INTRODUCTION

The rift that we intend to study crosses one of the largest endorheic basins of the world (2.5 million km^2), located in North-Central Africa between 8°–24° north and 6°–24° east, covering 8% of the surface area of the African continent, straddling Cameroon, the Republic of Chad, Niger, and Nigeria, and called the Chad Basin (Figure 1). The detailed geology of the area remains poorly known, and the Chad Basin is still almost unexplored with geophysical data. However, gravimetric studies began around 1952 when Lagrula (1952) conducts the first gravimetric acquisitions in which he discovers the existence of very important gravity anomalies. He interprets them only in terms of depth variation of crystalline rock basement, and this unfortunately led to conclusions in contradiction with geologic data. Therefore, Crenn (1955) carries out surveys around the southern and central areas of the Chad Basin. That investigation concludes with the discovery of a very significant negative gravity anomaly (Crenn, 1955). In 1956, D. A. Hansen (Louis, 1970) carried out limited studies of gravimetry and magnetism in five areas of central Chad for a water resource development program, but these gravimetric surveys were inconclusive. Only in 1959, significant gravity results in the Chad Basin were produced by the Office de la Recherche Scientifique and Technique d'Outre-Mer, now known as Institut de Recherche pour le Développement. Afterward, several geologic and geophysical studies were carried out in the framework of the project called "Contribution géophysique a la connaissance geologique du basin du Lac Tchad" by Louis (1970). Important efforts in understanding the crustal structures and

[1]University of Trieste, Department of Mathematics and Geosciences, Via Weiss 1, 34128 Trieste, Italy. E-mail: francesca.maddaloni@phd.units.it; tommasopivetta@yahoo.it (corresponding author); berg@units.it.

their geodynamic evolution were made by Fairhead and Green (1989) in which the authors interpreted the gravity anomalies as a combination of the effects of a sedimentary basin and a crustal uplift. Genik (1993) gives an overview on petroleum geology of the rift basins located in Niger, Chad, and the Central African Republic, based on the seismic reflection and well-log data of Exxon (1969–1991).

Our aim is to exploit satellite observed gravity data to characterize the rift basins overlapping the much broader intracratonic Chad sag basin in the west-central area of the African continent. To do this, we model the gravity field using all of the available constraints from the published morphology of the rift basin based on the interpolation of seismic profiles, published wells, and geodynamics. The results allow us to improve the understanding of rift structures in the West-Central African area, delivering a consistent crustal model compatible with all available data. The results suggest the presence of an extensive magmatic crustal intrusion below the rift basin, and in particular below the Termit Basin, presumably associated with the rifting phase, which has implications on the thermal evolution of the area.

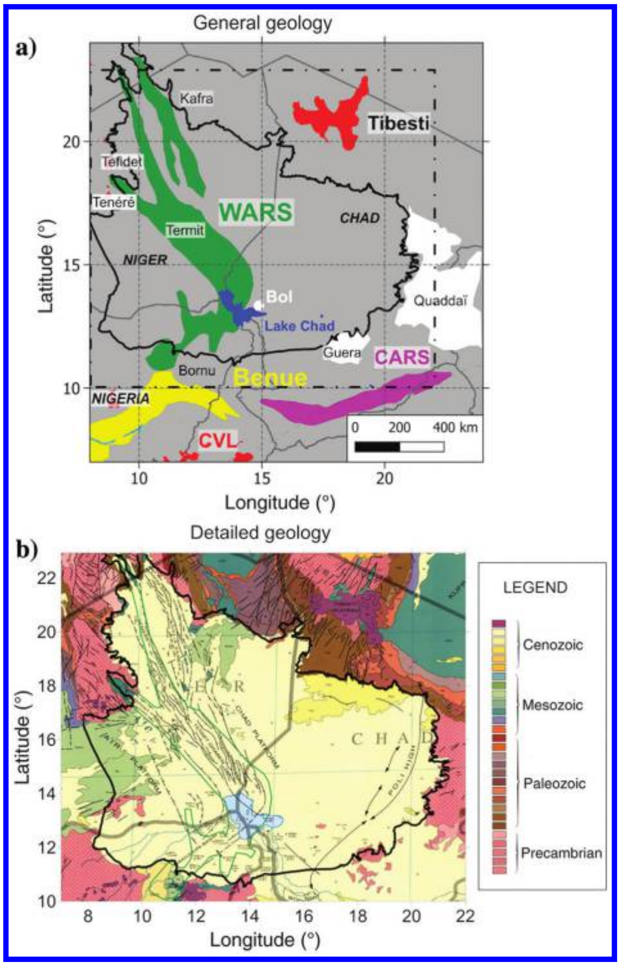

Figure 1. The Chad Basin geology. (a) The WCARS extension and location in the present period; WCARS is divided into the West African rift subsystem (WARS; the green areas) and the Central African Rift subsystem (CARS; the purple areas). The Benue trough outline is indicated in yellow; CVL, Cameroon Volcanic Line; white polygons, Precambrian massifs; and white dot, Bol stratigraphic well. The geologic boundaries are taken from Genik (1993). National boundaries are reported in gray. The dotted-dashed line bounds the area of the geologic map of (b). (b) The geologic map shows the lithologies that characterize the Chad Basin area (the black outline). Image modified from the International Geological Map of Africa (CGMW/UNESCO, 1990).

GEOLOGIC INTRODUCTION

The Chad Basin is considered as an intracratonic sag basin between the West African and Congo Cratons (Western block and Austral block) located on the Saharan Metacraton (Abdelsalam et al., 2002). The Saharan Metacraton comprises the Archean and Neoproterozoic continental domains, tectonothermally reworked by metamorphism during the Pan-African accretionary stage (Abdelsalam et al., 2002). The Pan-African consolidation crustal phase covered the time period 750–550 Ma (Genik, 1993), after which the area was a stable, mostly emergent platform (550–130 Ma). The lines of amalgamation have been thought to present lines of weakness, which gave the structure for the subsequent Cretaceous-Tertiary rifts (green, yellow, and purple areas in Figure 1a; Genik, 1993). The rifts are part of the West-Central African Rift System (WCARS) composed of the West African Rift System (WARS) and the Central African Rift System (CARS).

The Chad Basin is touched at its border by four major Precambrian massifs: the Mayo-Kebbi in the southwest, the Guéra in the south-center, the Quaddaï in the east, and the Tibesti in the north (Figure 1a and 1b). Geochronology has been obtained for samples from the Guéra massif and basement rocks of the Doba Basin of southern Chad (Shellnutt et al., 2017). The same publication attempted to give a timing of the magmatism of the region. Starting with the Early Cretaceous, the intracontinental rift system WCARS developed (Faure, 1962; Burke, 1976). The origin of WCARS is generally attributed to the breakup of Gondwana and the opening of the South Atlantic Ocean and Indian Ocean, leading to the fact that WCARS is associated with the Lower Cretaceous west African coastal rift basins, extending from Cameroon to Angola (Burke, 1976; Genik, 1993; Fortnam and Oguntola, 2004; Guiraud et al., 2005). The rifting of southwest Gondwana is divided into three main phases, the Berriasian (145–140 Ma), the Hauterrivian (135–137 Ma), and the Late Barremian to Early Aptian (130–125 Ma), which led to the formation of the Brazilian and African marginal basins, and the successive creation of the oceanic basement (Vidigal-Souza et al., 2020). Instead, WCARS continued to develop cycles of sedimentation during rifting, which did not succeed in a continental breakup. In fact, on the WARS, a first rift cycle extending throughout the Cretaceous included a rift phase extended from 145.5 to 99.6 Ma and postrift phase up to 65.5 Ma. During the postrift phase, volcanism has been reported from 96 to 88 Ma (Genik, 1993). Sedimentation during this first rift and postrift cycle was continental. The second cycle commenced with a rift phase from 65.5 to 23.0 Ma and a postrift phase up to the Quaternary, accompanied by volcanism. During the second rifting cycle, deposits are continental in WARS (Eastern Niger), which contains up to 10 km thick deposits (Genik, 1992). From Early Eocene, shorelines slightly regressed and a carbonate platform covered most of the marine domains (Wennekers et al., 1996).

The Chad Basin has been defined either as an oval-shaped sag basin, overlying the aborted rifts of the WCARS, or as an intracratonic rift basin, being part of the WCARS. The sedimentation commences toward the end of the first rifting phase of the WCARS.

A geologic synthesis of the Chad Basin is found in Moussa et al. (2013), who summarize previous publications. They present two orthogonal profiles crossing the entire basin, each extending over a distance of 700 km. The profiles extend in the southeastern and northeastern direction starting from Lake Chad, in which the borehole Bol (the white dot in Figure 1a), reaching the Precambrian basement at a depth of 450 m below sea level, is located. The sedimentary sequences of the Chad Basin are constrained by the borehole Bol and by the outcrops at the northern and southeastern margins of the Chad Basin. The deepest depocenter of the sag basin is below Lake Chad, and the sediment thickness smoothly diminishes toward the border of the basin from a thickness of 450 m. Above the Precambrian basement, a continental Cretaceous sandstone layer of up to 100 m is found, which is not well-defined in its age and fabric. The Miocene and Pliocene layers take up the greater part of the basin thickness and are constituted by continental eolian, fluvial or lacustrine deposits. As for the Cretaceous sandstones, the Miocene to Pliocene deposits are thicker below Lake Chad, and they smoothly decrease toward the border of the Chad Basin.

The basins of the WCARS have a totally different basin morphology compared with the Chad sag basin because they are much deeper, up to 10 km deep with steep normal faults (Figure 1b), and the greater part of the sediment layers are much older than the greater part of the sediments filling the Chad Basin. This points to two different mechanisms responsible for forming the basins belonging to the WCARS and forming the Chad sag basin.

The Bornu Basin in Nigeria, extending southward from the southern border of the Chad Basin, has a history recalling the evolution of WCARS, also recording the sedimentation between the Cretaceous and the Miocene, to the contrary of the Chad sag basin. The Bornu Basin joins the Benue trough and could be seen as the southward continuation of WCARS and connecting segment between WCARS and the Benue trough. The Bornu Basin has received recent attention due to the hypothesized presence of hydrocarbons (Wilson and Guiraud, 1992; Olabode et al., 2015; Suleiman et al., 2017). The stratigraphy is characterized by platform sedimentation due to rifting, with the first stages above a Precambrian basement belonging to Lower Cretaceous (Albian to Cenomanian) lacustrine and terrestrial deposits (Bima Sandstone). Estuarine-to-marine deposits follow (Cenomanian-to-Turonian; Gongila Formation), overlain by the marine shale unit (Fika shale). Estuarine-to-deltaic clastics (Maastrichtian; the Gombe Formation) overlie the shale. According to Olabode et al. (2015), the stratigraphic setting in the Bornu Basin up to the Fika Formation is slightly different, with sedimentation starting during the late Aptian-Albian. This formation is formed of sandstone deposited in a deltaic environment (the Bima Formation). Successively, a marine transgression occurred, connecting the Tethys and the South Atlantic, flooding the southern Chad Basin, leading to the shallow marine calcareous sandstones and shale (the Gongila Formation, upper Cenomanian-Turonian). A regression episode followed during the Turonian. During the Turonian-Senonian, a regressive phase estuarine/deltaic deposition in northeastern Nigeria formed the Gomba Sandstone. Then, a further transgression formed the open-marine shales, lasting from the late Senonian to the Late Cretaceous (Fika Formation). The transgression is related to tensional deformation of the Chad Basin lasting up to the end of the Cretaceous. The Kerri-Kerri Formation (Paleogene, nonmarine) was unconformably deposited above the shales. The Quaternary Chad Formation forms the youngest strata and consists of lacustrine and alluvial sedimentary deposits (Olabode et al., 2015; Suleiman et al., 2017).

General settings of the WCARS

One of the largest Cretaceous-Tertiary rift basins in WCARS is the Termit Basin (Figure 1a; called the Termit Graben in the geologic map shown in Figure 1b). It connects with the Tefidet Basin and Tenere Basin to the north and to the Bornu Basin in the south, at the northern end of the Benue trough (Figure 1a and 1b). The Termit Basin is an extensional asymmetric rift, 300 km long and from 60 to 110 km wide (Wan et al., 2014) and reaches an estimated maximum sediment thickness of approximately 12,000 m. It is underlain by the Precambrian Basement mentioned previously (Wan et al., 2014). These sediments comprise 300–2500 m of Lower Cretaceous terrigenous clastics, 800–4200 m of Upper Cretaceous shallow marine shales, sandstones, siltstones interbedded with minor carbonates and up to 350–2500 m Cenozoic continental sands, and shaly sediments.

In the Termit Basin, Eocene and Upper Cretaceous sandstones are the main hydrocarbon reservoirs. The oil discoveries from the Termit Basin mainly occur in the Eocene reservoirs and have been estimated to amount to more than 1 million tons of oil (Harouna and Philp, 2012). The hydrocarbons are mainly sourced from and sealed by Upper Cretaceous and Eocene marine and lacustrine shales (Genik, 1993; Harouna and Philp, 2012). Wells drilled in the northwestern continuation of the Termit part of the rift, included the Tefidet, Tenere, Kafra, and Grein basins, were unsuccessful in finding oil or gas and were dry (Genik, 1993). This shows a preponderance of hydrocarbon fields in the southern part of the WAR, with respect to its northern parts. Genik (1993) classifies two main oil families in WCARS: One type is derived from a marine-paralic source, and the second is derived from lacustrine sources. The overall geochemical characteristics of potential source rocks in the Termit Basin have been reported by Harouna and Philp (2012), and the detailed petroleum geochemistry of the Termit Basin has been defined by Wan et al. (2014).

Magmatism

In West and Central Africa, the magmatic activity associated with rifting stages are known from the Early Mesozoic (Triassic-Jurassic) to Cenozoic period (Wilson et al., 1998). This magmatism started from the progressive fragmentation of the Gondwana supercontinent during the Mesozoic (Guiraud and Maurin, 1992).

During the Cenozoic, magmatic activity has occurred within West and Central Africa, within the WCARS and outside it (Fleitout et al., 1986). Some other authors report that it is due to the reactivation of major deep-seated lithospheric fracture zones (Wilson et al., 1998).

In West Africa, the northwest–southeast-trending Ténéré, Termit, Tefidet, Grein, and Kafra Basins (WARS) of eastern Niger-Chad started rifting by Early Cretaceous (Genik, 1992; Guiraud and Maurin, 1992). The Termit rift basin is the largest basin in WARS, and for some authors it may have had continuous magmatic activity from Early Cretaceous to Holocene (Wilson and Guiraud, 1992). Therefore, within the northern areas of the Termit rift basin, the Neogene-Quaternary volcanism has been confirmed (Guiraud and Maurin, 1992). It is probably related to intraplate extension along northwest–southeast-trending structural lineaments that reach Lake

Chad (Pouclet and Karche, 1988). However, in the southern part of the Termit Basin, rhyolite and basalt dikes and dolerite sills from boreholes are constrained to be not older than 85–95 Ma (Genik, 1992). The Oligocene magmatic activity present along the Northern/Central African areas is more or less independent of the crustal extension phases (Guiraud and Bosworth, 1997). During the Neogene, the magmatic activity occurred in West, Central, and North Africa with volcanic fields concentrated in Pan-African mobile belts. Some authors associate the uplift of large dome structures of Neogene volcanic activity to the existence of a localized mantle upwelling (Guiraud and Binks, 1992).

DATA PRESENTATION

The data used to support our conclusions include potential field data, which we process in the framework of this paper, as well as seismic profiles that we find in publications. We process satellite and terrestrial gravity observations, which are complementary because they have different spatial resolutions. Furthermore, we use the basement depth of the sediment-filled rift basins based on active seismic investigations and recovered from literature. For reduction of the gravity field, we require sediment density changes with depth, which we obtain by applying constraints on the sediment porosity variation from well logs recovered in the literature.

Satellite gravity data

Satellite gravity data were used for calculating the free-air gravity anomalies and the complete Bouguer anomaly field. These are available in terms of the coefficients of the spherical harmonic expansion (SHE), which are then used to calculate the gravity field on or above the earth surface (Fecher et al., 2017). The SHE is divided into two types: satellite-only SHE, Goco-05s, and satellite-terrestrial combined SHE, Eigen-6c4 (Förste et al., 2014). The satellite-only data set has homogeneous errors due to the nature of the satellite acquisition but a limited spatial resolution of 80 km. In fact, the formulation of Goco-05s in terms of SHE uses the observed gravity field on board the satellite, using many cycles of the satellite orbiting around the earth, leading to a seamless coverage of the earth surface just leaving out an area close to the north and south poles. The second data set Eigen-6c4 has a higher spatial resolution of 10 km but suffers from possible localized errors in the terrestrial data and inhomogeneous data coverage (Bomfim et al., 2013) because the wavelengths smaller than 80 km stem from the terrestrial data. Where terrestrial data are lacking, topography has been used to generate fill-in gravity values (Pavlis et al., 2012). Fundamental for the use of gravity data is a digital terrain model, used to reduce the free-air gravity from the gravity effect of topography, obtaining the Bouguer gravity field. However, the topography is needed for calculating the isostatic compensation of the topography (Watts, 2001), with which the gravity values are reduced for the crustal density variations. In the present work, we use an aparametric substitute for isostatic compensation, based on the regression analysis between gravity and topography (Pivetta and Braitenberg, 2020), which has the advantage that no assumptions on the isostatic parameters are needed. We compare this new method to the classic isostatic reduction.

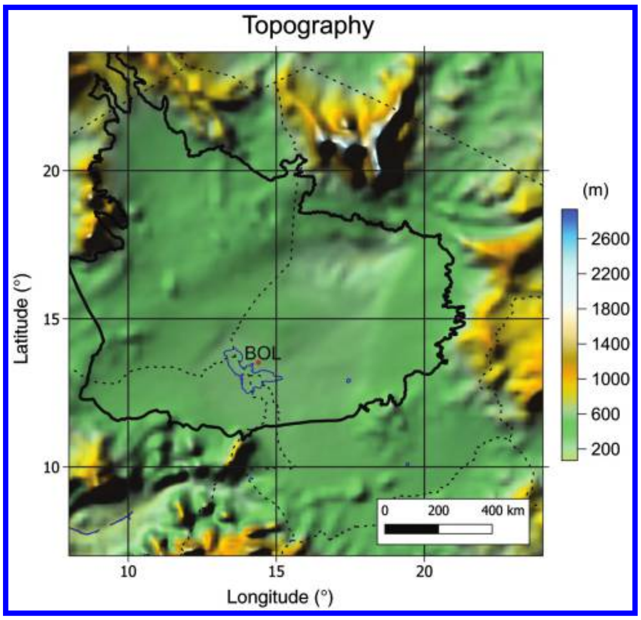

Figure 2. Topography map of the Chad Basin area (Etopo1). The solid black line marks the border of the Chad Basin, and the blue line marks the extension of Chad Lake. The city of Bol is the location of the stratigraphic well. Dashed black lines are national boundaries.

The Etopo1 is the digital terrain model developed in 2008 by the National Geophysical Data Center, an office of the National Oceanic and Atmospheric Administration (Amante and Eakins, 2009). It is available in SHE up to degree/order 2250 (Ince et al., 2019).

As displayed in Figure 2, the Etopo1 digital terrain map shows that the Chad Basin is essentially flat, especially in the central regions. The values of topography change from approximately 300 m inside the basin to 2600 m in a limited region of the northern areas.

The Goco-05s is the most recent SHE of the Goco-S series (Fecher et al., 2017). It has relatively high accuracy of 1 mGal globally and spatial resolution of 80 km, obtained from the combination of satellite gravity missions of the Gravity Field and Steady-State Ocean Circulation Explorer (GOCE), Gravity Recovery and Climate Experiment (GRACE), kinematic orbits (eight satellites), and Satellite Laser Ranging. It is available in terms of spherical harmonic approximation up to degree/order 280; the publishing year of the model is 2015 (Ince et al., 2019).

The term EIGEN is the acronym for European Improved Gravity Model of the Earth by New Techniques, and Eigen-6c4 is the latest release (2014) of the Eigen-6c-Series. It contains complete data of the GOCE mission and a combination of Laser Geodynamics Satellites, GRACE, GOCE, and terrestrial gravity data. It is a global combined gravity field SHE with accuracy close to a few mGal with maximum degree/order 2190 (Förste et al., 2014), which corresponds to a spatial resolution of 10 km. We calculate the free-air gravity anomaly following the definition of Barthelmes (2013). The Bouguer anomaly is calculated using the Etopo1 digital terrain model discretized in Tesseroids (Uieda et al., 2016) of constant density of 2670 kg/m^3 up to the classical Hayford radius of 167 km (Torge and Müller, 2012).

The free-air anomaly (Figure 3a) values change from −45 to 95 mGal; in particular, a positive localized feature is concentrated around the city of Fada in the northern part of the Chad Basin borders. The central regions of the basin are essentially characterized by values in anomaly that range from −45 mGal around the city of Faya-Largeau (northeast of the Chad Basin) to 35 mGal in the northwestern regions (the green areas). The Bouguer anomaly (Figure 3b) values range from −130 to 10 mGal, in particular, the positive localized anomaly is concentrated in the southwestern part of the map. The central regions of the basin are essentially negative with values of approximately −50 mGal. In some parts of the basin, there are localized anomalies with values of approximately −75 mGal (the light-blue areas). Over the Tibesti zone, near the city of Fada, the free-air gravity values are relatively high with positive values, whereas the Bouguer values take the most negative values of the study area. This is due to the positive correlation of the free-air gravity anomaly with topography and the negative correlation of the Bouguer field with topography, due to the isostatic compensation below the high elevation of the Tibesti Massif (TM) (Pivetta and Braitenberg, 2020).

The free-air anomaly (Figure 3c) values change from −60 mGal at minimum to 190 mGal at maximum. The central region of the basin now appears more detailed, despite the fact that the area is mostly positive with lower values of approximately 10 mGal. With the high spatial resolution of Eigen-6c4, it is possible to observe a particular positive anomaly around the cities of Mongo and Abéché that runs along the border between Chad and Sudan, called the banana high in Braitenberg et al. (2011). The Bouguer anomaly

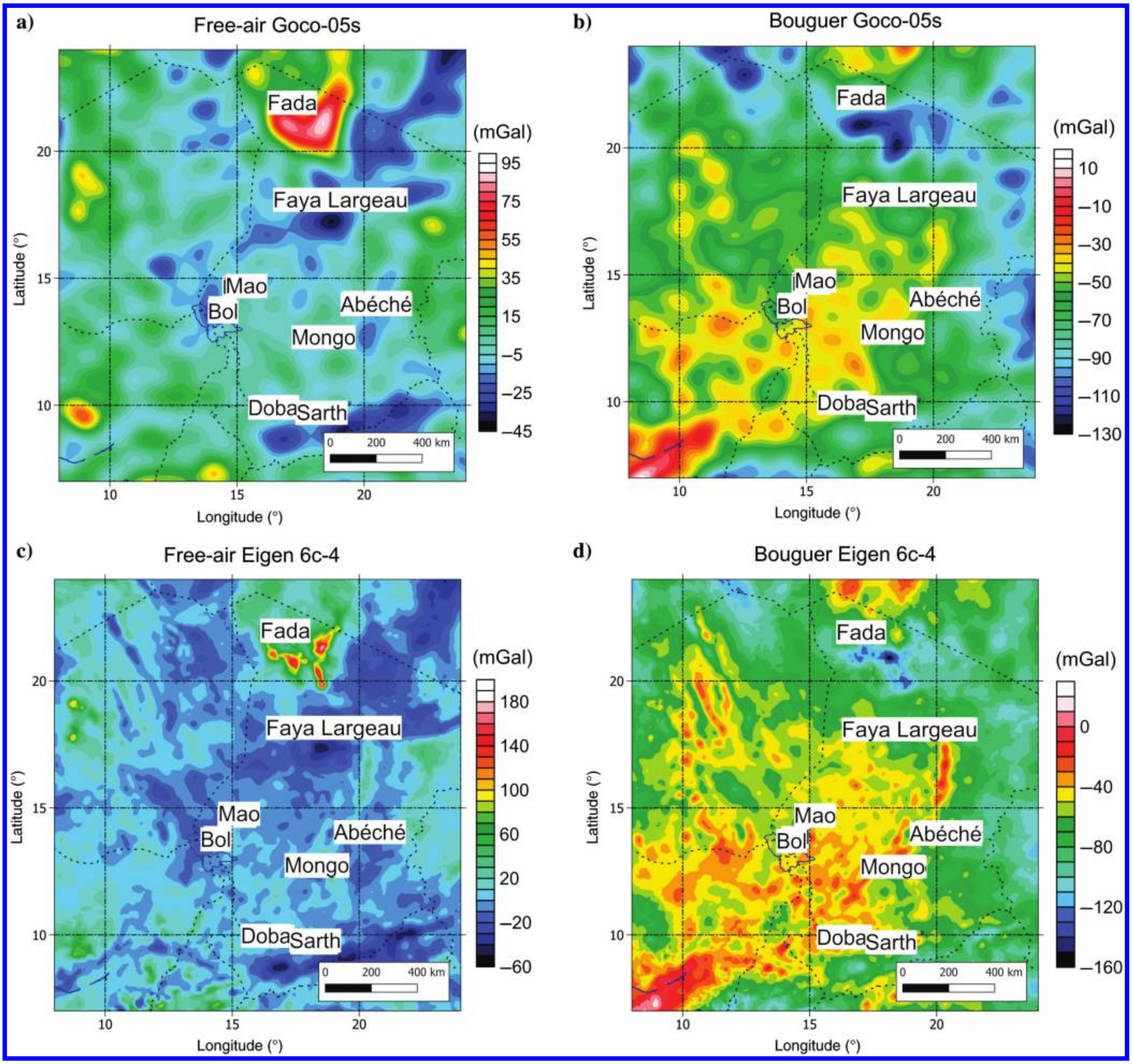

Figure 3. Gravity maps of the Chad Basin area for free air and Bouguer fields with two complementary models. (a) Free air from the gravity satellite-only data Goco-05s model with resolution of 80 km. (b) Bouguer gravity from the satellite-only data Goco-05s model with resolution of 80 km. (c) Free-air gravity from the combined satellite-terrestrial Eigen-6c4 SHE with resolution of 10 km. (d) Bouguer gravity anomaly from the combined satellite-terrestrial Eigen-6c4 SHE with resolution of 10 km.

(Figure 3d) values change from −160 to 20 mGal, and the positive localized feature is concentrated in the southwestern part of the map. The central region of the basin is essentially negative with values of approximately −60 mGal, and in some parts of the basin there are localized features with positive values of approximately 0 mGal (the red areas).

Terrestrial gravity data

The terrestrial free-air gravity data were retrieved at the Bureau Gravimetrique International (BGI), an agency created in 1951 by a decision of the International Union of Geodesy and Geophysics. It is one of the services of the International Association of Geodesy and the International Gravity Field Service. The central office of BGI is in Toulouse (France) (BGI, 2016). For the terrain data, the boundary of the survey area has the following coordinates:

1) latitude south 8°–north 20°
2) longitude west 10°–east 20°.

The free-air gravity values were reduced for the effect of topography in an analogous way as done for the gravity data retrieved from the global gravity SHE and detailed in the previous paragraph. The free-air anomaly values (Figure 4a) change from −55 to 70 mGal; in particular, the positive features are concentrated in the southwest between Cameroon and Nigeria. The anomalies in the central region confirm the existence of a tectonic structure north of Lake Chad. There is a localized region of positive anomaly around the city of Mao not seen before in the other maps. Being an isolated feature, it cannot be excluded from being a measurement error. The high is not seen in the Goco-05s map, but the resolution is lower and cannot show isolated anomalies. Confirmation can be obtained by new measurements over the area. The negative values of free-air anomaly around the city of Faya Largeau are confirmed. The Bouguer anomaly (Figure 4b) values change from −100 to 10 mGal, in particular, the positive features are concentrated in the southwestern part of the map. The central regions of the basin are essentially negative with values of approximately −40 mGal; in some parts of the basin there are isolated areas with values of approximately −75 mGal (the light-blue areas). The free-air and Bouguer gravity field confirm some evidence of density structures connected to tectonic features, which will be discussed in the following sections.

Benefits versus disadvantages of satellite and terrestrial data

Although some common features are evident in the three gravity data sets that we used, namely, the extreme values of free air and Bouguer fields over the Tibesti area, differences between the SHE formulations are evident. The satellite-only SHE Goco-05s, with its homogeneous accuracy, is useful for checking terrestrial data and finding outliers and comparing the long-wavelength field above 80 km. On the contrary, the Eigen-6c4 combined SHE (satellite and terrestrial) has a higher spatial resolution than the Goco-05s SHE, but it has an inhomogeneous quality of data because it presents errors from the terrestrial data within it. Finally, the terrestrial data have a very high spatial resolution where they were acquired and stations exist, but the station distribution is inhomogeneous. For the remainder of the work, we use the gravity field derived from the Eigen-6c4 SHE.

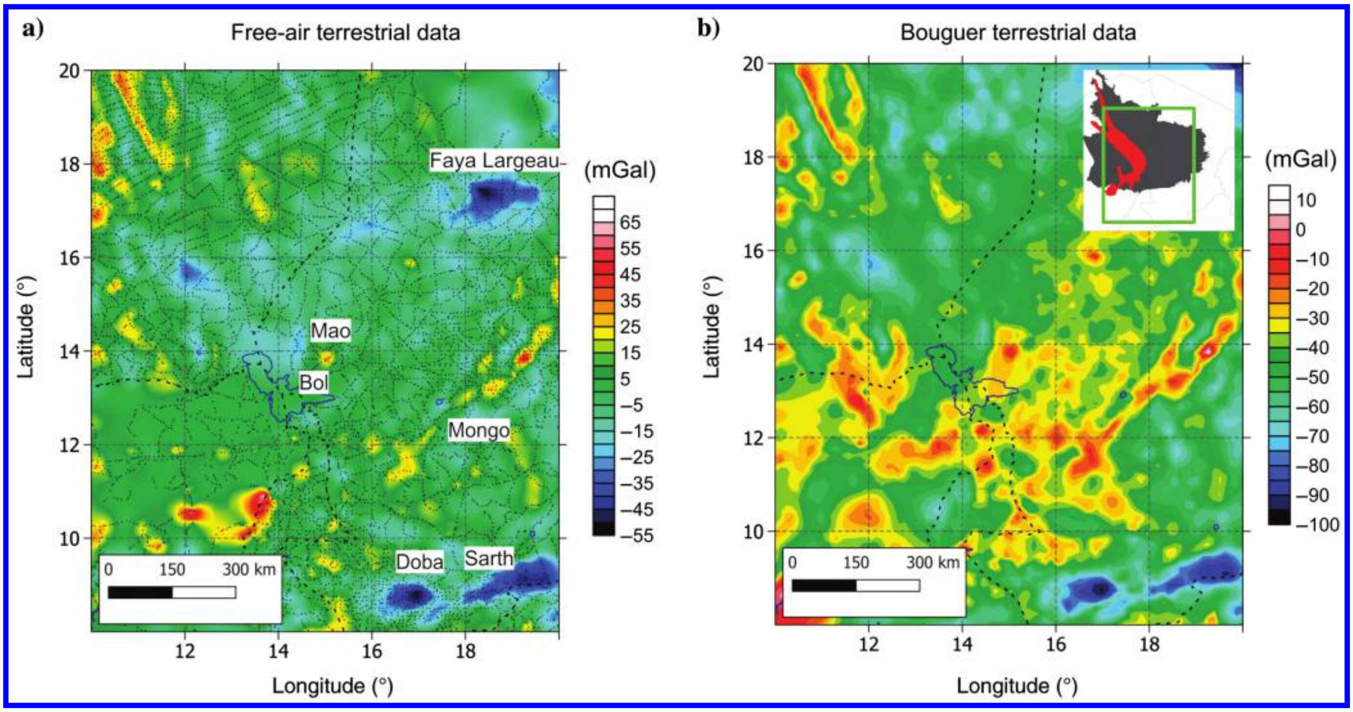

Figure 4. The gravity field of the Chad Basin area derived from terrestrial data of BGI. (a) Free-air gravity anomaly map and (b) Bouguer gravity anomaly map. The inset in (b) shows the location of the terrestrial data of BGI (the green rectangle) with respect to the Chad Basin (in dark gray).

Seismic and well-log constraints for the gravity modeling

In the past few decades, the Chad area was geophysically explored in the frame of a hydrocarbon exploration project by Exxon and its partners from 1969 to 1991, Texaco then Esso surveys from 1970 to 1980, and Conoco in 1975. Elf took part in exploration surveys in 1980. The results of the exploration campaigns are summarized in the work of Genik (1993), who gives an overview of the petroleum geology of the rift basins in Niger, Nigeria, and Chad.

Many different wells in the area of WCARS give us information about the basement rocks and sediment lithology inside the rift basins of the Ténéré, Termit, and Grein/Kafra Basins. An exhaustive list of the wells, including metadata as the year of acquisition, the name of the well, and the essential data including the maximum depth, the age of the formations, the lithotypes, and coordinates of the well position are given in Appendix A. Summarizing the information, it is found that the rocks consist of granites, pegmatites, gneisses, hornfels, quartzites, granodiorites, and schists of Pan-African age. The oldest sediments within the rifts were drilled in the Ténéré Basin, where a prerift Permian Triassic assemblage is made up of 930 m of continental deposits (Genik, 1993). From the wells, we were able to constrain the porosity variation with depth, which is needed to constrain the sediment compaction and consequent density variation with depth, needed to calculate the gravity effect of the sediment layers during the forward-modeling step.

The acquired seismic information allowed Genik (1993) to develop a map of the sediment thickness in the rift of the WCARS by analyzing several seismic reflection profiles. The detailed seismic profiles are unavailable to us, whereas the sediment thickness is published in Genik (1993) in the form of isopachs, which we have digitized and georeferenced, as shown in Figure 5. The variation of the sediment thickness is closely related to the rift structures of the WARS (Figure 5). This sediment thickness model is used to constrain our gravity models during the forward modeling and the inversion steps.

PROCESSING OF GRAVITY DATA

The method used to process the gravity data is divided into two main processing steps defined by (1) removing the isostatic component from the observed Bouguer gravity data using a regression analysis between the topography and the gravity field (Pivetta and Braitenberg, 2020) and (2) removing the gravity effect of sediment layers through a forward-modeling approach. In the following, we first give an overview on the regression analysis method and its application to the study case. We also present a comparison with a more commonly used methodology for the computation of isostatic residuals. The final section illustrates the correction for the sediment effects.

Regression analysis: Theory

The regression analysis between the topography and the gravity field is an alternative method to the classical isostatic residualization in the Chad Basin area (Braitenberg et al., 2013; Braitenberg, 2015; Pivetta and Braitenberg, 2020). It is based on the theory of isostatic compensation of a thin plate through the flexure of the lithosphere. This plate is approximated to an elastic body overlying an inviscid fluid (Watts, 2001). Toward increasing wavelengths and decreasing equivalent elastic thickness, the flexural response tends toward the Airy local isostatic compensation mechanism. According to the Airy hypothesis and assuming that the Bouguer gravity field is dominated by the crustal isostatic compensation, the relation between the Bouguer field and an opportunely low-pass filtered topography is almost linear. The need to filter the topography arises from the different wavelength content between the gravity and topography fields and, in particular, because gravity acts as a low-pass filter on the source density distribution. In addition, usually the earth's gravity field is known at a lower spatial resolution with respect to the topography.

To show the principle of the regression analysis, we consider the Bouguer anomaly over an area as being due to the sum of the gravity effects of an Airy root, approximated through the Parker formula (Blakely, 1995) truncated at the first order and of small gravity perturbations uncorrelated to the isostatic effects (ε). In formulas, this reads

$$BG(k_x, k_y) \approx -2\pi G R(k_x, k_y)(\rho_m - \rho_c)e^{-k_r tc} + \varepsilon, \qquad (1)$$

where ρ_m and ρ_c are the mantle and crust densities, respectively, tc is the reference depth of the Moho (e.g., 35 km), $R(k_x, k_y)$ is the 2D Fourier transform of the Airy root undulation calculated from the reference depth tc, k_r is the radial wavenumber defined as $\sqrt{k_x^2 + k_y^2}$, and G is the gravitational constant (6.674×10^{-11} $\mathrm{Nm^2/kg^2}$). The function $e^{-k_r tc}$ is known as the earth filter (Blakely, 1995). The Airy

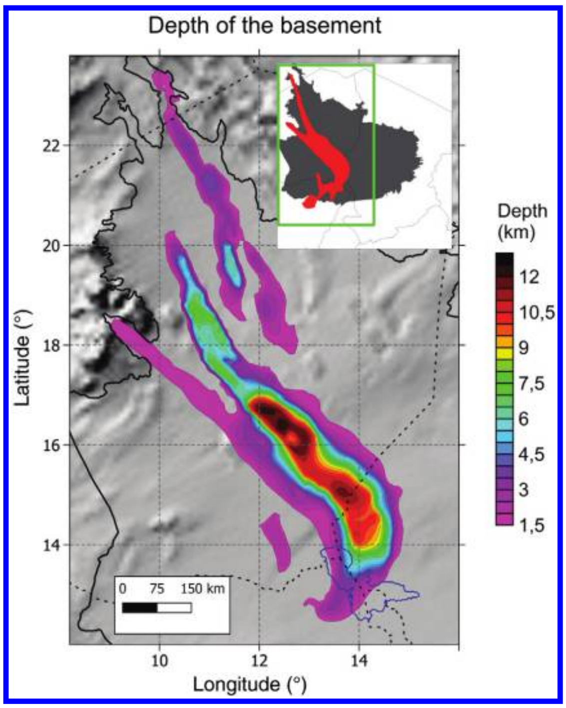

Figure 5. Depth of the basement referred to mean sea level shown with the color scale superposed on the shaded relief (Etopo1). The depth model is taken from the interpretation of exploration geophysics surveys in Niger, Nigeria, and Chad (Genik, 1993). The solid black line is the Chad Basin, and the dashed black lines are the national boundaries. The inset shows the location of the map with respect to the Chad Basin (in dark gray) giving its outline with the green rectangle. The WARS extension is indicated in red.

root undulation $R(k_x, k_y)$ is related to the Fourier transform of the topography through the following equation 2:

$$R(k_x, k_y) = H(k_x, k_y)\frac{\rho_c}{\rho_m - \rho_c}. \tag{2}$$

Inserting $R(k_x, k_y)$ into equation 1, we finally obtain a relation between the Bouguer and a low-pass filtered topography:

$$BG(k_x, k_y) \approx -2\pi G H(k_x, k_y)\rho_c e^{-k_r tc} + \varepsilon. \tag{3}$$

If we go back to the spatial domain, equation 3 becomes

$$BG(x, y) \approx -2\pi G\rho_c h(x, y) * \mathfrak{F}^{-1}\{e^{-k_r tc}\} + \varepsilon. \tag{4}$$

In equation 4, we see that $h(x, y)$, the inverse transform of $H(k_x, k_y)$, is convolved with $\mathfrak{F}^{-1}\{e^{-k_r tc}\}$, which is the inverse Fourier transform of the earth filter. The filter is a low-pass filter; the cut-off wavelength depends on the reference depth tc. If instead of the Airy mechanism we consider a flexural response of the Moho, a further low-pass filter is applied to the topography (Figure 6a).

For the purposes of the regression analysis, it is important that all of the high-frequency content of the topography, not involved in the isostatic process, is filtered out. For this reason, a spectral analysis between gravity and topography is performed to define the filter cut-off wavelength. Optimal filter parameters can be obtained by comparing the gravity and topography radial averaged spectra and in particular by inspecting spectral attributes such as coherence (Figure 6b and 6c; Kirby, 2014). In our study case, to filter the data, we use a Gaussian filter that represents a good approximation of the combined effect of earth and flexure filters (Figure 6a).

Once the topography has been filtered, the regression analysis can be performed over extended areas, retrieving a unique regression equation, or in alternative, exploiting sliding windows, which allow obtaining spatial variations of the regression parameters.

From the regression analysis, we expect to observe anticorrelation between the Bouguer gravity and the filtered topography and hence negative slopes of the regression lines; variations in the absolute value of the slope can be observed over areas with systematic crustal density variations or in response to lateral changes in the isostatic mechanism (Pivetta and Braitenberg, 2020). A limit case, for instance, is when the topography is completely uncompensated (i.e., high elastic thickness), and in that case the regression slope is close to zero.

From the regression analysis, we can calculate the residual values, which can be considered as a type of isostatic residuals. The mathematical explication of residual values is expressed by the formulas

$$BG_{\text{reg}}(x, y) = mh(x, y) + q \tag{5}$$

and

$$BG_{\text{res}}(x, y) = BG_{\text{obs}}(x, y) - BG_{\text{reg}}(x, y), \tag{6}$$

where $BG_{\text{obs}}(x, y)$ is the observed Bouguer anomaly, m is the angular coefficient of the regression line, $h(x, y)$ is the low-pass-filtered topography, q is the value of the line intercept, and $BG_{\text{reg}}(x, y)$ is the expected Bouguer from the regression relation. So far, we have assumed that the gravity field of the root is approximated by a Parker expansion (Parker, 1973) truncated at the first order: Neglecting the higher order terms in the Parker expansion leads to the appearance of gravity residuals in regions with steep topography. This is not an issue in our study area in any case because the area is mostly flat with long-wavelength gentle topographic expressions.

The advantage of the regression method resides in being almost aparametric, requiring only the definition of the filter parameters that are in any case estimated by the data themselves. This is an advantage compared to the more classic isostatic anomalies, which require assumptions on the mantle and crustal densities as well as the elastic thickness, Poisson's ratio, and Young's modulus. The method has been successfully applied for studying other areas such as the Alps (Braitenberg et al., 2013), Africa (Braitenberg, 2015), the Southern Atlantic and South America, and on Mars (Pivetta and Braitenberg, 2020).

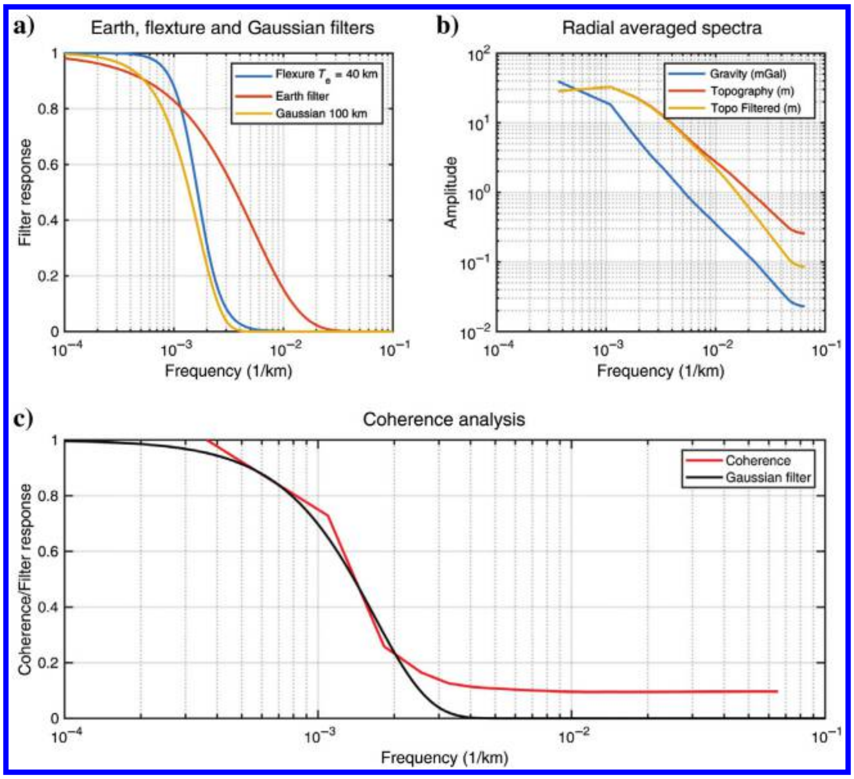

Figure 6. Spectral responses of the earth filter and the flexure process. (a) Transfer functions of the earth filter (reference depth = 30 km), flexure filter (Te = 40 km), and a Gaussian filter that approximates the combined effect of the former ones. The Gaussian filter cut-off wavelength corresponds to 100 km. (b) Radial averaged spectra of the Bouguer anomaly, topography, and filtered topography for the study area. The cut-off wavelength of the Gaussian filter applied to the topography is 100 km. (c) Coherence attribute for the study region and the response of the Gaussian filter used for filtering the topography before the regression analysis.

The regression analysis is considered to be a good methodological choice in our study case because it is particularly suitable for studying geophysically poorly known areas such as the Chad Basin. In our case, the regression analysis between topography and gravity has two scopes, which are

1) to determine the anomalies due to the upper crustal mass inhomogeneity, reducing the Bouguer anomaly for the effect of crustal thickness variations
2) to characterize the crustal units and define tectonic boundaries which produce the different correlation behavior between topography and gravity.

Preprocessing phase: Spectral analysis and filtering

As already hinted, the spectral analysis is a prerequisite for performing the regression analysis, in particular, we need to filter out the high-frequency contents from the topography not involved in the isostatic process; not considering a filtered topography would introduce high-frequency signals into the residual gravity field compromising the further analysis. The filter needs to take into account the lower resolution of the Eigen-6c4 SHE data with respect to the topography, as well as the effect of the two filters illustrated previously.

The Eigen-6c4 SHE is published with a maximum degree of $N = 2159$, which corresponds to a wavelength of $\lambda = 40{,}000/2159$ km $= {\sim}20$ km. The spatial resolution of the field is given by half of the smallest resolved wavelength of the field (Barthelmes, 2013). We chose to use a maximum degree $N = 2159$, lower than the expansion of $N = 2190$ because, for degrees greater than 2159, the error on the coefficients of the SHE is larger than the coefficient itself, whereas limiting the expansion to $N = 2159$, the errors are smaller than the coefficients. However, we found that a realistic resolution, based on the average spacing of the terrestrial data, is lower — between 50 and 100 km.

To take into account such differences in the spatial resolution as well as the action of earth and flexure filters, we performed a spectral analysis between the two fields. Figure 6b reports the radial averaged spectra of the topography (orange) and gravity (blue), which are then used to compute the coherence (Figure 6c). From the coherence, we estimate the optimal cut-off wavelength for the Gaussian filter, which is 100 km. In our case, we defined the cut-off wavelength λ so that at 6λ the response of the filter is 1.523×10^{-8}. As we will see in the next section, the goodness of fit the filter choice is confirmed by a comparison between the regression residuals and the isostatic residuals calculated according to more commonly used approaches that assume Airy and flexure mechanisms.

In Figure 7a and 7b, the effect of low-pass filtering the topography is seen with the filters of 100 and 200 km. The filter with 100 km cut-off wavelength is ideal for the comparison with Eigen-6c4, whereas the filter with 200 km is good for the Goco-05s field.

Processing step 1: Regression analysis and isostatic residuals

The results of regression analysis tests in the Chad area produced the regression line reported in gray in Figure 8a. Although the data points are scattered with respect to the regression line, the error of the slope is small (two orders of magnitude smaller). The slope is -6.44×10^{-2} mGal/m $\pm\, 3.90 \times 10^{-4}$ mGal/m, and the intercept is 29.8 mGal $\pm$ 0.08 mGal. For low topography (<1000 m), we have a homogeneous regression coefficient that would correspond

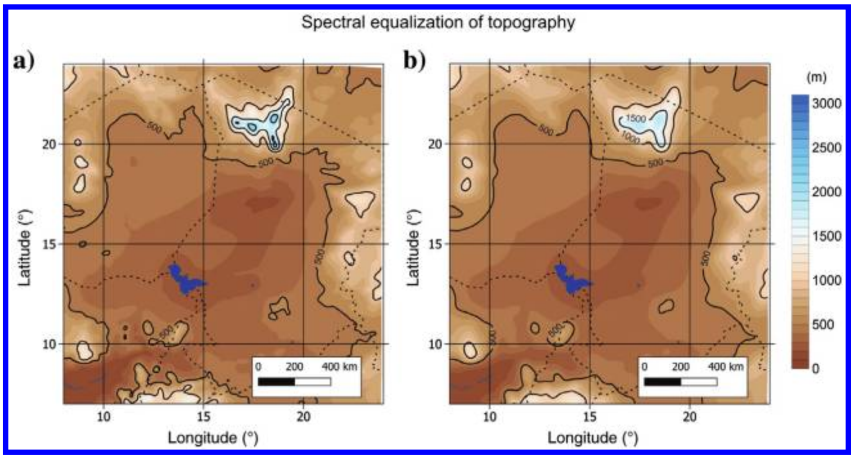

Figure 7. Spectral equalization of topography to the gravity fields by low-pass filtering. (a) The topography at the cut-off wavelength of 100 km and (b) the smoothed topography at the filter wavelength of 200 km. An appropriate filter for the spectral equalization of topography to the Eigen-6c4 model is 100 km.

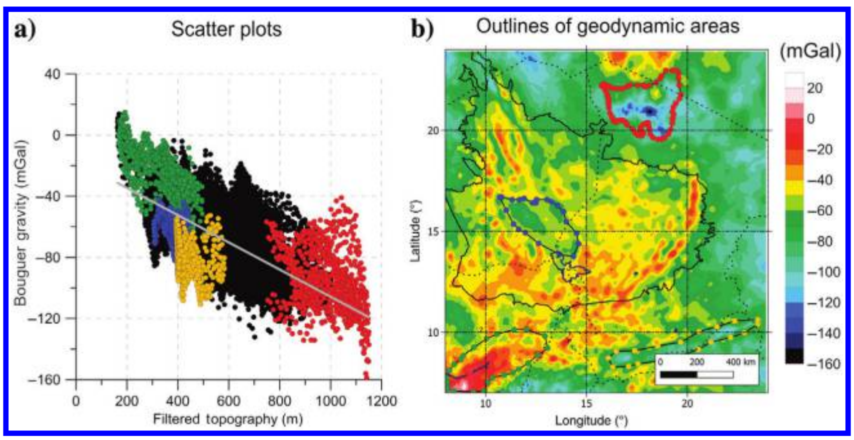

Figure 8. Regression analysis in the Chad Basin. (a) Scatterplot of the Bouguer gravity anomaly and filtered topography in the Chad Basin and the surrounding areas; linear regression line reported in gray. The colored dots show the scatter points from different areas reported in (b) with the same color code. The black dots are all of the remaining areas of the map. (b) The outlines of different geodynamic areas superposed on the Bouguer anomaly map: green, the Benue trough; blue, WARS; red, Tibesti; yellow, CARS; the dark blue outlines, Lake Chad and the Benue River; the dashed black lines, political boundaries; and the Chad Basin outline is shown with the solid black line.

to a uniform isostatic compensation mechanism and the absence of superficial density inhomogeneity. For higher topography (>1000 m), the correlation is loose, with more positive gravity values than expected. If we consider that the highest topography is limited to the volcanic TM, this indicates that the topographic elevations of the massif have higher density than the average density in the area. In Figure 8a, the scattered points from the Tibesti area are shown in red.

In the study case characterized by a sedimentary basin with flat topography, the Bouguer field is increasingly negative toward the center of the basin and the presence of the basin can be identified by the negative deviation of the gravity signal from the average regression line (Braitenberg, 2015). This behavior is identified by the blue and yellow dots in Figure 8a of the scatterplot, which represent the sedimentary basins located in WARS and CARS.

On the contrary, the Benue trough is associated with higher values with respect to the regression line; this is probably due to an important magmatic activity associated with this rift basin (Eyike and Ebbing, 2015). The residual gravity values (Figure 9a), obtained by equation 6, represent the gravity anomalies due to geologic features inside the Chad Basin. Practically, they are all the points plotted in Figure 8a that are not fitted by the regression line.

They represent local anomalies of gravity not related to the isostatic effects. To test the validity of the regression method and the gravity residual results on the study area, we analyzed the behavior of gravity, residuals, and topography along a profile AB that transversally crosses the entire Chad Basin (the trace in Figure 9a).

The graph in Figure 9d shows that the area along the profile is topographically flat with highest values that correspond to the TM. The Tibesti zone is characterized by a strong negative Bouguer anomaly field certainly due to the crustal roots of the massif. The isostatic effect along profile AB (the red curve in Figure 9c) is the effect of deep crustal bodies that we wanted to mitigate using the regression analysis. To understand the effect of the uncertainty on the slope on the final residual values (Figure 9b), we calculated them by varying the slope parameter adding and subtracting its standard deviation. The standard deviation between the different residual maps is very small (± 0.75 mGal); this proves that the residual values calculated in the study area are stable and are reliable for further analysis.

The reliability of the residual map is further tested with a comparison with more classic approaches for calculating the isostatic anomalies. Figure 9e and 9f plots the isostatic anomalies calculated from Airy and flexural models in which we assumed standard crustal and mantle densities (2670 and 3200 $\mathrm{kg/m^3}$, respectively), a reference depth of 30 km, and an elastic thickness $Te = 40$ km in case of flexure. Such a Te is consistent with the coherence analysis and is in agreement with dedicated studies over the Chad area (Eshagh and Pitoňák, 2019).

We observe a generally very good agreement between the regression residuals and Airy and flexural anomalies for what comprises the pattern and the amplitude range of the anomalies; the most striking differences are found in the Tibesti region and the Benue trough (Figure 10a and 10b). Here, however, we also observe important differences between the Airy and flexural responses (Figure 10c). Regarding the areas of the Chad Basin, the differences between the models are very small, generally less than 5 mGal and mostly affecting the very long wavelength components as shown by the maps of differences in Figure 10a and 10b.

Along the profiles (Figure 10d) traced in the Chad Basin area (the traces in Figure 10a and 10b), we also note that the high-frequency content of the various residual fields is identical, further proving that the regression analysis has not introduced any spurious high-frequency distortion in the area of interest. Because we have good constraints on basin geometry and petrophysical properties of the Tefidet and Ténéré Basins based on the work of Genik (1993), we proceeded to calculate the gravity effect of the basins and compare them with the residual maps.

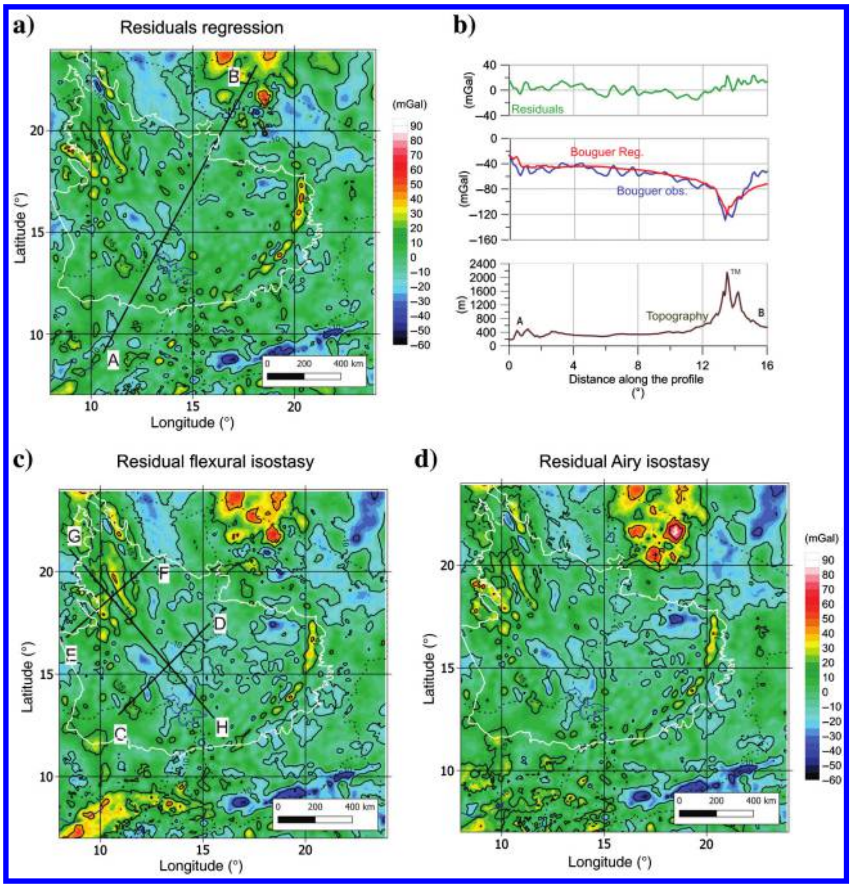

Figure 9. Residuals comparison. (a) Gravity residual map resulting from the regression analysis (BG_{res}). Profile AB crosses the entire basin. (b) The gravity residuals curve; TM, Tibesti Massif. (c) The comparison of the Bouguer anomaly field (Bouguer obs.; BG_{obs}) versus the isostatic effect, estimated through the regression analysis (Bouguer reg.; BG_{reg}). (d) The topography variation along profile AB. (e) Gravity residual from a classic Airy residualization. (f) Gravity residual assuming flexural isostasy with $Te = 40$ km. In maps, the white outline denotes the Chad Basin.

Processing step 2: Gravity forward modeling: The gravity effect of sedimentary layers

The first aspect to consider when modeling the gravity effect of sediments is to estimate the density as a function of depth. According to the compaction law models, we know that the density values of the rock are strictly dependent on their porosity and the change in function of the burial depth. The porosity decays exponentially with depth with the formula (Allen and Allen, 2013)

$$\varphi(\gamma) = \varphi_0 e^{-c\gamma}, \tag{7}$$

where φ_0 is the surface porosity, γ is the depth, and c is the decay constant (porosity-depth coefficient). The bulk density (ρ_b) of the porous rock is expressed by the formula

$$\rho_b = \varphi(\gamma)\rho_f + (1 - \varphi(\gamma))\rho_{ma}, \tag{8}$$

where $\varphi(\gamma)$ is the porosity, ρ_f is the average density of the fluid occupying the pore space, and ρ_{ma} is the average density of the rock matrix. In this study case, we used the data that come from well logs information (Genik, 1993).

We analyzed the porosity variation with depth (Figure 11) by fitting the observed data with an exponential curve, obtaining a value of surface porosity of $\varphi_0 = 0.5$ and a decay constant of $c = 0.47\ \text{km}^{-1}$. The depth-dependent density profile is then

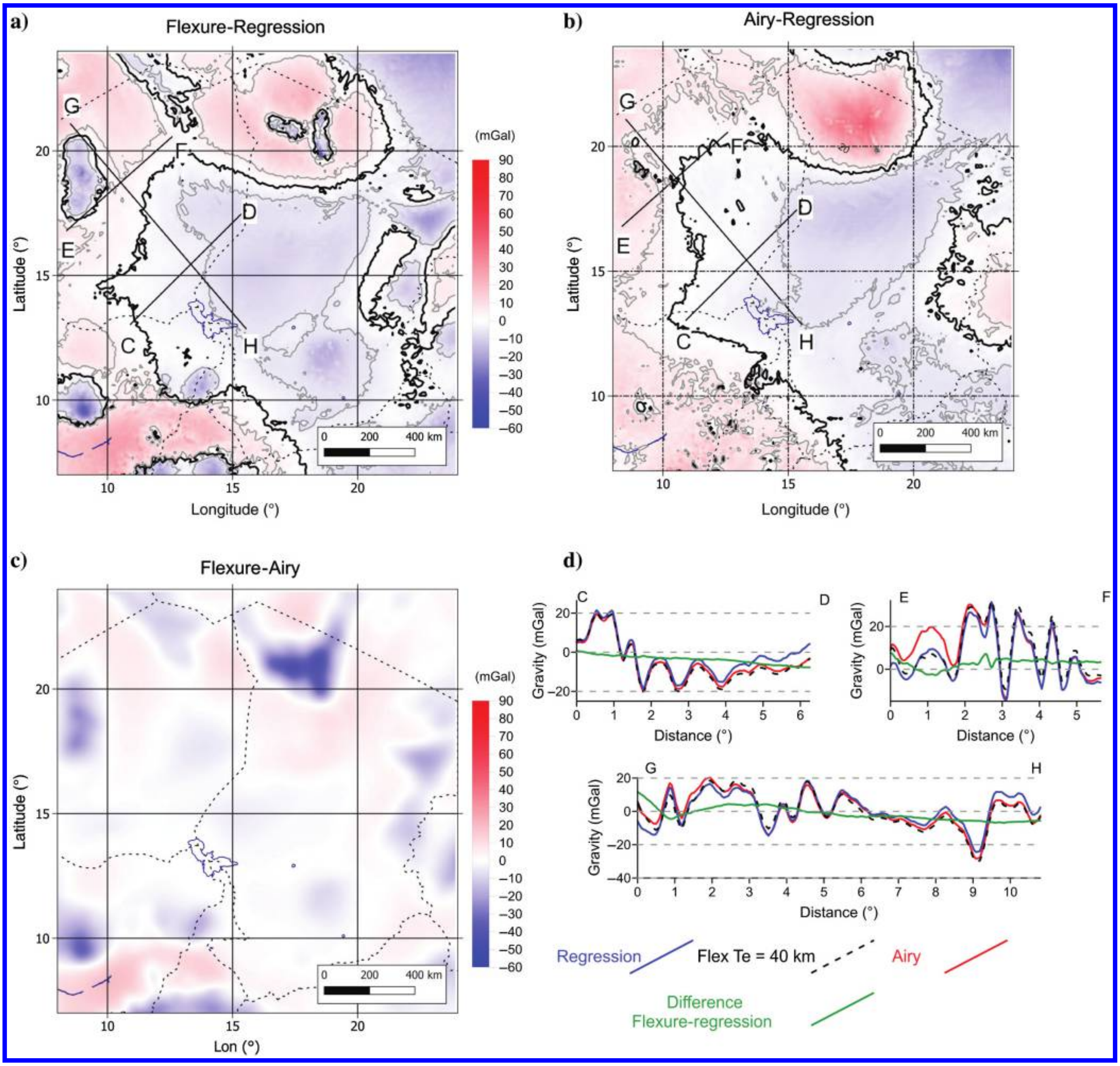

Figure 10. Comparison of residuals from regression analysis and isostatic classic models. (a) Difference between the gravity isostatic anomalies calculated assuming a flexure mechanism (Te = 40 km) and the regression residuals: black contour, 0 mGal anomaly; gray contours, ± 5 mGal; dashed lines: national borders. The locations of the profiles are shown by the straight black lines. (b) The same as (a) but for the Airy isostasy. (c) Differences between the gravity effects of the Airy and flexural isostatic responses in the study area. The range of the color axis is the same as in (a and b). (d) Comparison along the profiles; traces of the profiles are shown in (a and b).

calculated assuming the density of the fluid inside the pores to be $\rho_f = 1000\ \mathrm{kg/m^3}$ (water) and the density of sedimentary rock matrix to be $\rho_{ma} = 2450\ \mathrm{kg/m^3}$. For the gravity calculation, we need the density contrast of the sediments against the reference density, which is set equal to the standard density used for the reduction of topography ($2670\ \mathrm{kg/m^3}$). We calculated the depth density profiles from 0 to 12.5 km according to deepest points in the seismic section (Genik, 1993). The entire sediment volume is discretized with spherical prisms, also called tesseroids (Liang et al., 2014). The tesseroid is defined by the areal extent in longitude and latitude and the depth extent with the top and bottom. The size of the tesseroid was 10 km in longitude and latitude. We use the software routines of Uieda et al. (2016) for calculating the gravity field for one tesseroid. The gravity effect of all sediment layers is obtained by dividing the sediment volume into a series of tesseroids, assigning the density defined by the above procedure, and summing the gravity effect of all tesseroids. This allows us to produce a 3D density model of the entire area of the rift basins and consequently calculate the gravity effect of the sediment layers along the WARS (Figure 12).

Processing step 3: Comparison between gravity residuals and the gravity effect of sediment layers

To test the validity of our work, we compared the observed Bouguer gravity, reduced for the isostatic compensation, here calculated through the regression analysis (BG_{res}) (Pivetta and Braitenberg, 2020), with the gravity effect of sediments. Assuming that the initial values of sediment thickness from the exploration surveys (Genik, 1993) are correct, and asserting that the sediment density is constrained from the wells, the Bouguer residual from the regression analysis should display a gravity minimum comparable to the gravity effect of the sediments. As shown previously, the sediment basin reaches 12 km thickness, which is expected to produce a pronounced gravity minimum in the residual Bouguer values emerging from the regression analysis. If the residual Bouguer values do not present the expected sediment gravity low, that implies the presence of an increased density somewhere in the crust that compensates the sediment gravity effect. We proceeded removing the gravity effect of sediments (G_{bas}) from the gravity field residuals (BG_{res}), resulting in the gravity residual map of Figure 13a. In the same figure, two profiles AB and CD that cross, respectively, the northern and the southern areas of WARS (Figure 13a) are shown, along which

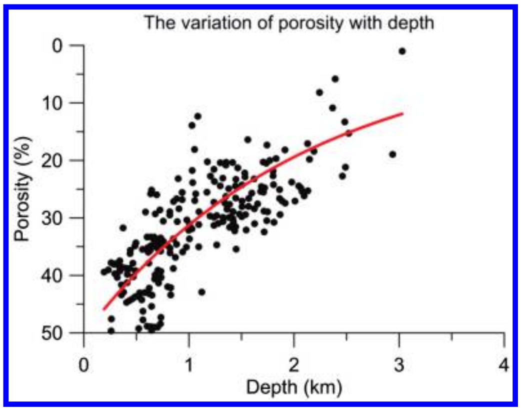

Figure 11. The variation of porosity values with depth along the WARS (Genik, 1993).

we trace the Bouguer gravity result of the regression analysis (BG_{res}) and the gravity effect of the sediments (G_{bas}).

As shown in Figure 13a, the characteristic of the gravity field changes considerably as we move from north to south along WARS. Along the AB profile, the minima found by the sediment modeling have also been found on gravity residuals of the regression analysis, although the sediment gravity values are more negative compared with the Bouguer residual values. On the contrary, in the southern areas of WARS, along profile CD, there is no correspondence between the modeled effect of sediments and the residual gravity anomaly (Figure 13c). Here, the modeled field of the sediments is close to −40 mGal more negative than the observed field. For this fact, it was necessary to introduce new crustal density anomalies in addition to the sediments.

Modeling of magmatic intrusion along the southern area of WARS

Removing the gravity effect of sediment G_{bas} from the Bouguer regression residual gravity values (BG_{res}), a large positive anomaly below the WARS results (Figure 13b), which resembles the outline of a lobster and which we call the “lobster high” (G_{lob}). The tail marks an elongated gravity high, and the lobster arms and head mark three subparallel highs, oriented consistently in the northwest–southeast direction. According to geologic references, this positive anomaly trend could be inferred to represent a crustal density anomaly associated with the Mesozoic rifting activity.

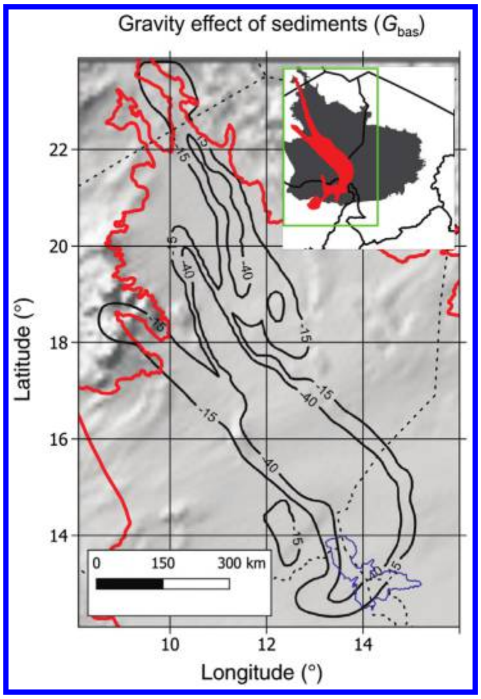

Figure 12. The gravity effect of sediment layers according to the information taken from exploration geophysical surveys (Genik, 1993) superposed on the shaded relief map of the topography (Etopo1). Red lines: borders of the Chad Basin; dotted gray lines: political boundaries; solid gray line: Lake Chad; and solid black lines: gravity isolines (mGal). The inset shows the location of the area with respect to the Chad Basin outline. The inset shows the location of the map with respect to the Chad Basin (dark gray) giving its outline with the green rectangle. The WARS extension is indicated in red.

With these premises, the next step we made is to perform an inversion modeling of the positive residual gravity values to identify the possible volume and areal extent of the causative body. For the inversion, we consider three possible solutions: one shallower, resembling a crustal intrusion, a deeper one, which could be interpreted as a magmatic underplating with crustal thinning, and, finally, a combination of both. The inversion is done by an iterative procedure in which the inversion is performed in the spectral domain and the forward calculation is made in the spatial domain with prisms (Braitenberg and Zadro, 1999). The iterative method has some similarities with the iterative method of Oldenburg (1974) in the sense that the inversion step is the same, in which the gravity field is inverted to a sheet mass positioned at a given reference depth through the first linear term of the Parker series expansion of the gravity field in the spectral domain. The sheet mass is expanded to a physical thickness setting a given density, and then the gravity field of this mass is calculated through the discretization in the prisms. The gravity residual is obtained and inverted through the linear Parker term to update the sheet mass, and this process is iterated. In the Oldenburg (1974) method, the forward-calculated gravity field in the iterations is obtained through the nonlinear terms of the Parker series expansion (Parker, 1973). The two methods lead to approximately the same results because the Parker series expansion gives nearly the same gravity effect of the mass as the gravity effect of the mass calculated through the discretization through prisms.

The bottom of the inverted body is assumed to be flat and is set to the reference depth, and only the top of the body is defined through the inversion algorithm. The results depend inverse linearly on this density contrast, a smaller contrast requiring a greater thickness of the body (Braitenberg and Zadro, 1999; Braitenberg et al., 2000). The depth of the body influences the solution because a deeper body requires a greater thickness to explain the starting gravity signal.

A conceptual illustration is shown in Figure 14, in which the essential elements of our model are given with the sediment basin in green, the crustal underplating/thinning in orange, and the upper crustal intrusion in yellow. Two end-member models are defined with an intrusion at the upper crustal level (Figure 14a) and one at the Moho level with crustal thinning (Figure 14b); furthermore, we considered a mixed model (Figure 14c), which is a combination of the former two.

The first solution assumes a typical density contrast between intrusive basic rocks and the granitic basement of 300 kg/m^3 and a bottom depth of 20 km. Figure 15a shows the gravity residuals of the inversion procedure for the shallow mass: The standard deviation of the residuals is 3 mGal. The resulting top depth of this magmatic intrusion is plotted in Figure 15b.

The second solution that interprets the positive signal as being due to a deeper crustal source starts from a reference depth of 35 km and assumes a higher density contrast of 400 kg/m^3. This solution could be interpreted in geodynamic terms as an underplated magmatic zone with a crustal thinning associated with the rifting process (Allen and Allen, 2013). Figure 15c and 15d reports the gravity residuals and the depth map of the top interface of the underplated body, respectively.

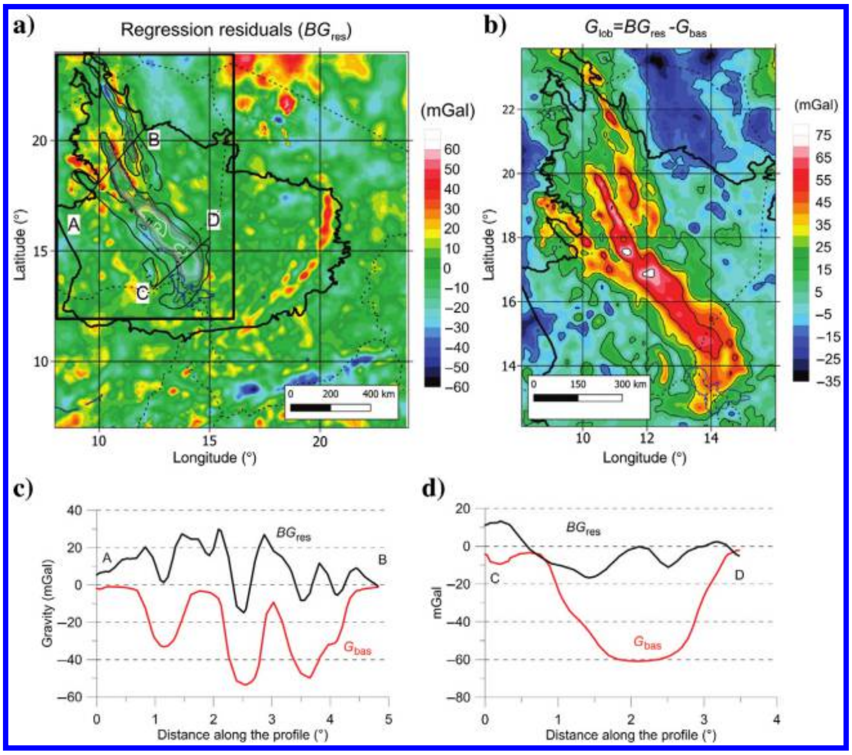

Figure 13. Comparison between the Bouguer gravity residual values (BG_{res}) and the gravity effect of the sediment thickness along WARS. (a) Bouguer gravity residual map (from regression analysis, BG_{res}) and the localization of two profiles AB at the north and CD to the south. (b) Map of the gravity values corrected for topography, isostatic compensating mass result of the regression analysis and sediments, removing the component due to the gravity effect of the sediment thickness (G_{bas}) from the Bouguer regression residuals (BG_{res}). (c) Comparison of the Bouguer regression residuals and the gravity effects of sediments on profile AB. (d) The comparison of Bouguer regression residuals and the gravity effects of sediments on profile CD.

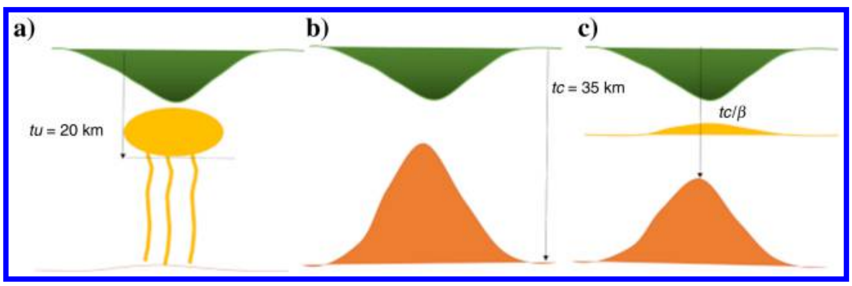

Figure 14. Illustration with the three conceptual models. (a) Sediment basin and shallow magmatic intrusion. (b) Sediment basin and crustal thinning. (c) Sediment basin, shallow intrusion, and crustal thinning with magmatic underplating: Tu, reference depth for the shallow mass; tc, reference depth for the lower mass; and tc/β, crustal thickness after stretching. Descriptions of these parameters are detailed in the text.

In this case, the standard deviation of the residuals is 6 mGal. The reduction of the root-mean-square (rms) amplitude of the gravity field at each iteration step is shown in Figure 15f.

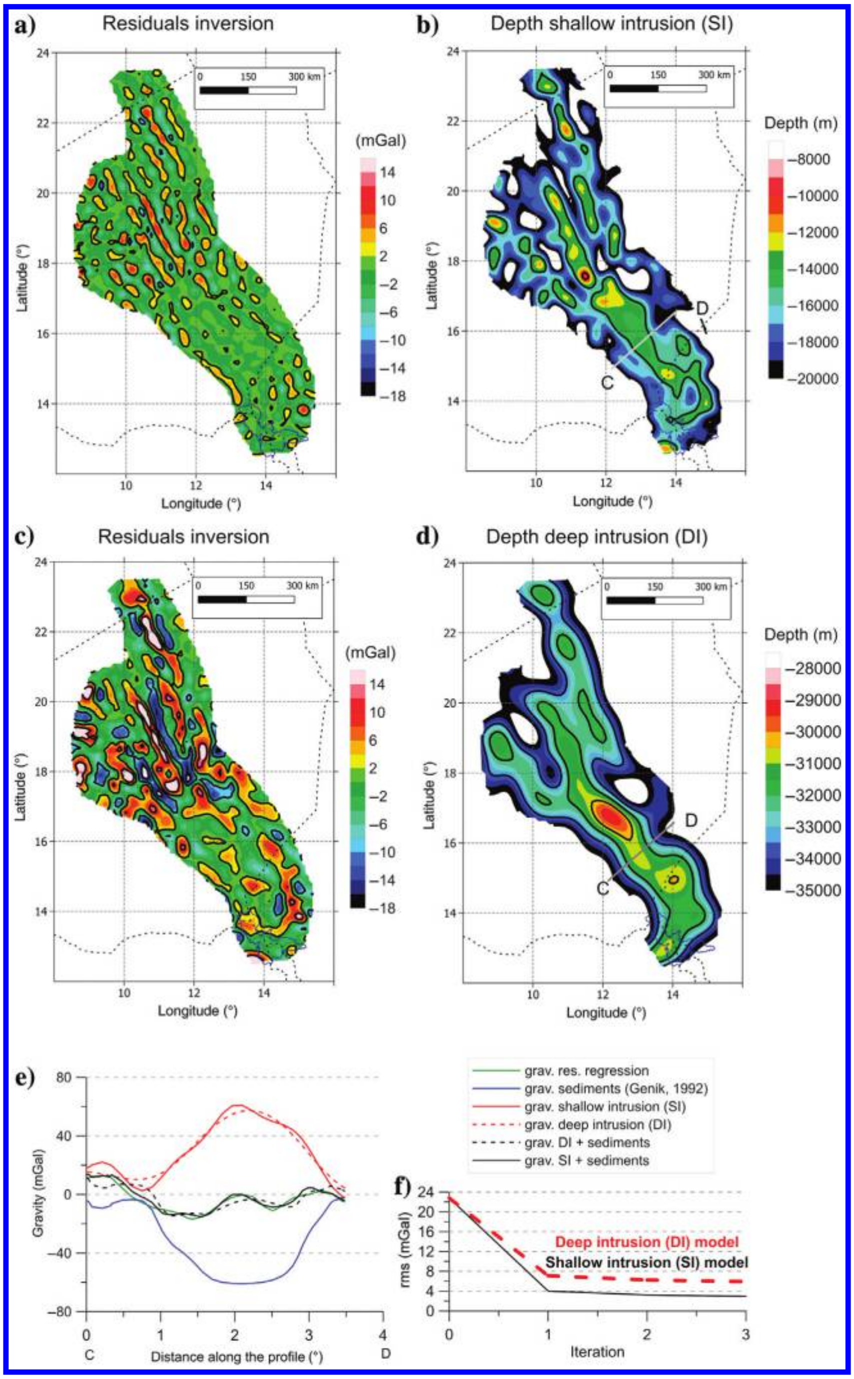

Figure 15. Inversion modeling on WARS. (a and b) The results for the "crustal intrusion model": (a) shows the gravity residuals of the inversion, whereas (b) shows the top depth of a shallow intruded body; (c and d) are the same but for the deep intrusion model. The black line in (b and d) shows the trace of the profile reported in (e). (e) Profile crossing the WARS basin: The green line is the residual derived from the regression analysis, the blue line is the sediment gravity effect, and the red line is the gravity effect of the shallow crustal intrusion (the solid line) and deep intrusion (the dashed line). The dashed black line is the sum of the sediments and the deep intrusion effect, whereas the solid line is the same but considering the shallow intrusion. Both density models fit the observed regression residuals (the green line). (f) The rms error versus iterations of the inversion: black line, the shallow intrusion model; red line, the deep intrusion model.

Both of the examined solutions fit the observed gravity data well, as evidenced by comparing the green and black profiles in Figure 15e. In this figure, the green curve represents the observed residual, the solid black line is the effect of the crustal density model that includes the sedimentary basin and the crustal intrusion, and the dashed line reports the sediment model effect together with the underplating/crustal thinning effect.

Comparing the residual maps of the two solutions we may state the following: The underplating model (Figure 15c) shows several high-frequency residuals with amplitudes exceeding 20 mGal. These signals are clearly attenuated in the shallower solution, where the residuals barely reach 10 mGal. Not having further constraints, both solutions are valid, and the underplating and shallow intrusion models are well capable of explaining the long-wavelength part of the lobster high.

The shallow solution could be a package of basalt flows at the bottom of the Termit Basin that are not reached by the available wells and which are confused with basement rocks by seismic interpreters. This situation would be similar to what is seen in the aborted rifts of the West Siberian basin, where the basalt has been reached by the wells, and the location has been hypothesized to be present at the bottom of the sedimentary sequences revealed by the seismics (Vyssotski et al., 2006). Such basalts, if completely buried, may have escaped notice by geologists. In this case, there would be no contribution from a deep crustal intrusion or crustal thinning and the magma feeders reaching the mantle would not significantly contribute to the gravity signal.

In a more plausible scenario, the lobster high is produced by a combination of relatively shallow and relatively deep sources that contribute to the observed gravimetric signal. In fact, if there is a pile of basalt present below the sediments, this implies a correspondingly significant volume of mafic intrusive rocks at greater depths within the crust. Because we do not have constraints on the minimum plausible depth for these rocks, we show the results of one possible combined model. The gravity field G_{lob} could be divided in a certain proportion $ul = u/(1-u)$, between the field generated by the upper and lower masses, resulting in the two fields $G_{\mathrm{lob}} = G_{\mathrm{lobup}} + G_{\mathrm{loblow}} = uG_{\mathrm{lob}} + (1-u)G_{\mathrm{lob}}$ corresponding to the field generated by the upper and lower masses. For each of the upper and lower gravity residuals, the masses could be inverted, leading to the combined effect of a superficial and deep mass. The value $u = 0$ corresponds to the end member of the underplating/crustal thinning, whereas $u = 1$ corresponds to the pure shallow intrusion model. Therefore, it can be expected that the value of u is smaller than one and greater than zero.

To reduce the ambiguity of the solutions, we explored the relationships among the partition coefficients, density contrast, and thickness of the deep intrusion/Moho uplift. The deep mass could be a combination of crustal thinning and underplated crustal mass according to the McKenzie and Bickle (1988) model, in which the authors calculated the fraction of melt produced during a lithospheric extension. The melt production critically depends on the stretching factor (β) and on the thermal conditions prior to the rifting phase.

We analyze the effect of the partition coefficient on the final result by choosing the characteristic wavelength (λc) and its amplitude (Ac) of the residual field, which, according to the profile in Figure 15c are approximately $\lambda c = 200$ km and $Ac = 60$ mGal, and by calculating the corresponding thickness of the upper and lower masses, respectively, for the different density contrasts $\Delta\rho$ as

$$\Delta Hl \approx \frac{uAc10^{-5}}{2\pi\Delta\rho G e^{-\frac{2\pi}{\lambda c}tc}} \tag{9}$$

and

$$\Delta Hu \approx \frac{(1-u)Ac10^{-5}}{2\pi\Delta\rho G e^{-\frac{2\pi}{\lambda c}tu}}, \tag{10}$$

where tu and tc are the reference depths of the upper and lower masses. The formulas give the thickness of the upper ΔHu and lower ΔHl masses for the characteristic wavelength of the Southern Termit Basin (profile CD in Figure 15b and 15d). We further define the stretching factor through $\beta = tc/(tc - \Delta Hl)$ because in this case we interpret ΔHl as the crustal thinning that accompanied the rifting and gave room for the deep mass. This would follow the model of McKenzie and Bickle (1988).

In Figure 16, we give the stretching factor and thickness of the upper mass for three plausible partition factors u = 0.2, 0.1, and 0.05, for varying density contrast at the lower crustal and upper crustal levels, respectively. The density contrast covers a range of values expected for a basaltic intrusion against crustal density values of various composition. The values chosen for the inversion of the single-wavelength ($\lambda c = 200$ km) gravity anomalies are 35 km for tc and 20 km for tu. The stretching factor decreases for an increase of the density contrast of the lower mass (because β depends on the thickness of it), and it is higher for the lower partitioning coefficient u. The thickness of the upper mass is lower for a higher density contrast and a lower partitioning factor.

According to the McKenzie and Bickle (1988) model, β should be approximately 1.5 or greater to produce a significant melt of a few kilometers, under the condition of normal sublithospheric temperature and average lithospheric thickness. Therefore, in our case, we prefer a low partition coefficient of less than 0.1 and a density contrast of the lower intrusion of less than 400 kg/m^3 to obtain a β value able to produce a nonnegligible amount of melt. In our model, the melt produced by adiabatic decompression during the rifting partially ponds at the base of the crust and partially reaches the upper crust feeding a subbasin magmatic intrusion. We speculate that such differentiation produces a restitic underplated mass with density similar to the lower crust; the enriched part constitutes the upper intrusion.

On the basis of these above considerations, we performed the inversion assuming $u = 0.1$, which attributes 10% of the gravity signal to the upper masses and 90% to the deep intrusions. For the upper intrusion, $\Delta\rho$ is set to 300 kg/m^3 whereas the lower mass has a density contrast of 400 kg/m^3. Figure 17 shows the geometry of the intrusions assuming a bottom of the mass at 35 km (Figure 17a) and 20 km depth (Figure 17b) for the deep and shallow masses, respectively. We see that generally the deeper intrusion is several times thicker than the shallow intrusion.

The presence of a crustal intrusion is not evident in the WARS area from other geophysical studies (i.e., seismic); however, as already pointed out, magmatic deposits have been sampled in the area. In the Benue trough, Eyike and Ebbing (2015) model a similar gravity high with a combination of shallower magmatism and underplating. The shallower source explained the high-frequency part of the gravity field, whereas the underplating contributed mostly at low frequencies. Because no further independent constraints are available up to now, we cannot completely rule out each of the three hypotheses, but we find the combined model to be the more plausible from a petrological point of view (McKenzie and Bickle, 1988).

DISCUSSION

WCARS is one of the most important tectonic structures of the Central Africa zone. The western side extends over hundreds of kilometers from Nigeria and Niger, down to southern Chad and Northern Cameroon (Binks and Fairhead, 1992; Guiraud and Maurin, 1992). The area pertains to the former Gondwana continent, which from Mesozoic time was affected by continental extension with the formation of wide stretch basins. These basins

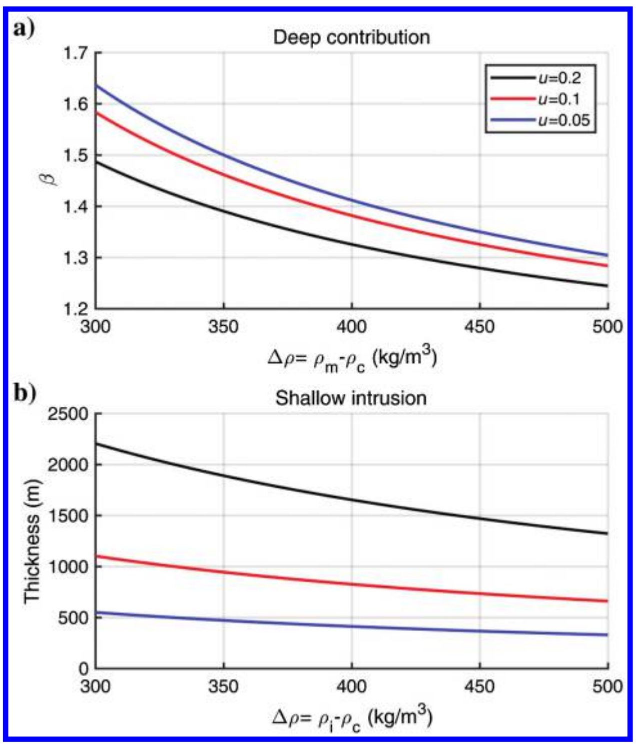

Figure 16. Exploring the effect of partitioning factor u. (a) The stretching factor as a function of the density contrast of the lower mass for three different partition factors u = 0.2, 0.1, and 0.05. (b) Thickness of the upper mass as a function of density contrast for three different partition factors u = 0.2, 0.1, and 0.05.

propagated inland from the successful rifts that led to the opening of the Atlantic Ocean and the separation of Africa and the Americas.

Different studies in the past have been carried out for the reconstruction of crust and mantle structures of WCARS, and most of them relied on the interpretation of seismic and terrestrial gravity data along profiles (Browne and Fairhead, 1983; Stuart et al., 1985; Dorbath et al., 1986; Fairhead and Okereke, 1987; Plomerová et al., 1993; Fairhead et al., 2013). Up to now, a 3D model of the crustal bodies, constrained by seismic and the satellite gravity data of GRACE and GOCE, has only been available for the southern sector of WCARS and the Benue trough (Eyike and Ebbing, 2015). In this study, the authors were able to depict the main crustal features of the system such as the magmatic underplating and the associated thinned crust exploiting a forward-modeling approach of the EGM08 gravity model.

Detailed 3D modeling of the recent satellite gravity fields, constrained by the available seismic and well data, is however lacking for the WARS, and our work aims at filling this gap. The analysis was carried out taking advantage of the recent gravity potential SHE formulations Eigen-6c4 and Goco-05s. One major problem is the signal separation generated by the crustal thickness variation from the signal generated by the shallower crustal units; by shallower units we mean the subsurface density inhomogeneities related to the rifting process. Given the scarcity of information on crustal thickness from independent geophysical investigations for studying the structures of the rift basins of the WARS, we exploit the regression method between the Bouguer gravity field and the topography (Pivetta and Braitenberg, 2020). This method allows us to remove the isostatic signals from the observed gravity field and to produce a first gravity residual map. The observations derived from the Goco-05s SHE were used to check and validate the long-wavelength signals in the Eigen-6c4 SHE; meanwhile, the terrestrial data were used to confirm the existence of localized positive/negative gravity anomaly trends due to geologic structures. The cumulative errors on Goco-05s SHE derived products are homogeneous in space with values of approximately 4 mGal (Braitenberg, 2015). The anomalies that we discussed and interpreted have amplitudes of more than 80 mGal and wavelengths of approximately 300 km, so they are clearly greater than the instrument noise of the satellite gravity mission. The residual maps showed that the negative gravity anomalies correlated with the basin structures over the Tefidet, Grein, Kafra, and Ténéré Basins. However, the Termit rift basin displayed near-zero anomaly values. We corrected the residual maps for the sediment contribution using a basin model derived from the literature (Genik, 1993). The sediment density model is constrained by a seismic thickness model and a density conversion of a fitted porosity curve derived from well-log data. The gravity effect of the sediments fits the gravity residuals well in the northern basins, whereas in the south (the Termit rift basin) the residuals reveal a broad positive gravity anomaly of more than 80 mGal in amplitude. The uncertainty of the seismic sediment thickness can not explain such a broad anomaly; in fact, assuming a 5% error of the depth values, the maximum error of the base of the sediments would be approximately 1 km. This corresponds to a gravity variation of approximately ±2.5 mGal. In addition, the uncertainty on the fitted porosity curve could contribute with an additional ±2 mGal. Consequently, the maximum value of the uncertainty over the entire study area reaches only ±8 mGal. From all of these considerations and assuming that the exploration geophysics contributions are of high quality, which are mostly proprietary and not available externally (Eyike et al., 2010), we find that the broad positive gravity residual below the Termit rift basin could not be due to artifacts in the gravity data or in the sediment modeling.

Therefore, we inverted this gravity high in terms of a dense body below the WARS basins, according to the presence of long-wavelength anomalies that some authors relate to the presence of a mantle uplift (Gibb and Thomas,

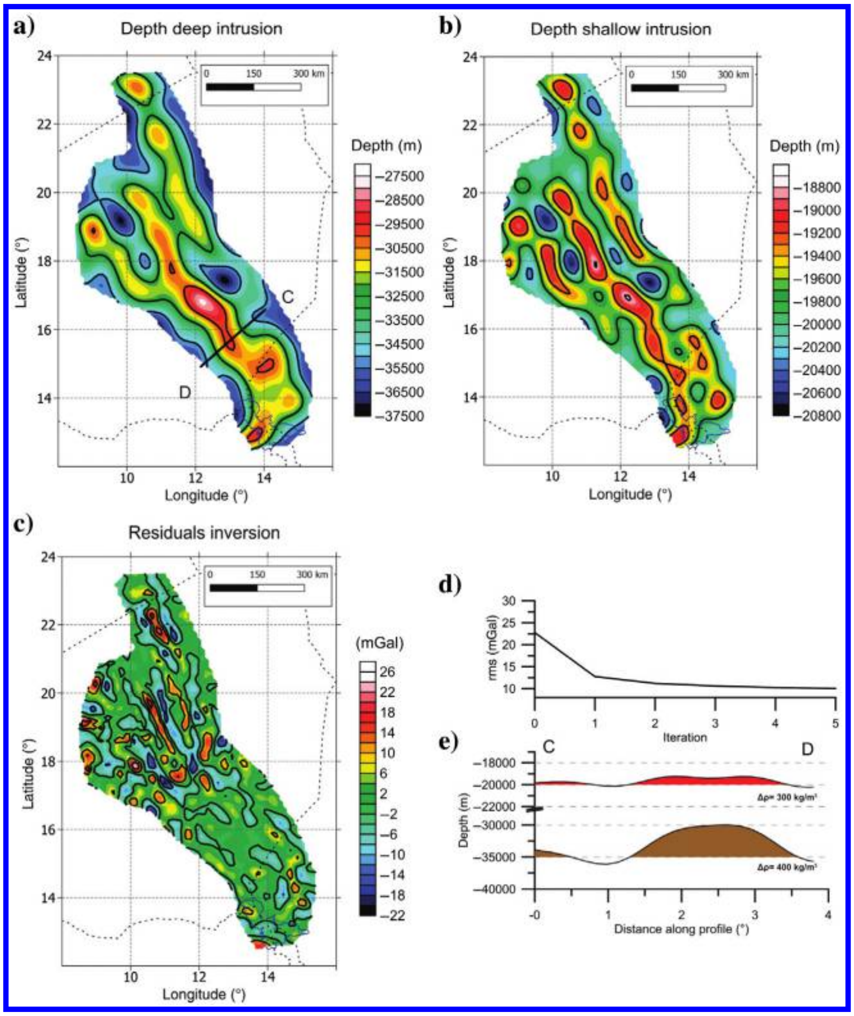

Figure 17. Combined inversion with shallow and deep inverted masses. (a) Depth of the top of the deep mass, (b) depth of the top of the shallow mass, and (c) final residual of the combined model. In all plots, the national boundaries are shown with the dotted lines. (d) The rms error at various iterations during the inversion. (e) Crustal cross section of the upper and lower masses along profile CD. The position of CD is plotted in (a).

1976; Fountain and Salisbury, 1981; Fairhead, 1986; Fairhead and Okereke, 1987). We considered two end-member models and a combination of them, a shallow solution simulating a subsurface magmatic chamber and a deeper solution that involves a lower crust intrusion (underplating) associated with crustal thinning.

The shallower model is able to better explain the high-frequency features of the inverted gravity signal; however, considering the long-wavelength contributions in the lobster high, a deep source is also able to reproduce the observed gravity signal. Considering the shallower solution, if we assume a density contrast equal to $\Delta\rho = 300\,\mathrm{kg/m^3}$ and a reference depth of 20 km, we obtained a continuous magmatic intrusion of approximately 10 km thickness. Decreasing the contrast of the density, the dimensions of the magmatic intrusion increase unrealistically.

The deeper solution would be compatible with the geodynamic context of crustal thinning combined with deep magmatism, both associated to the rifting phase: Our calculation predicts that the mass anomaly could be up to 8 km thick. We remark that high-frequency anomalies in the gravity residuals are hard to explain with such distant sources.

An alternative solution is to divide the gravity signal between a source below the rift sediments and at the lower crust, which would lead, for instance, to a shallow source of approximately 1 km thickness and a deep source of approximately 7 km. An uncertainty of ± 8 mGal, divided according to the partition coefficient u, leads to an uncertainty in the inverted thickness of ± 1.3 km for the deeper contribution and of ± 0.15 km for the shallow one.

In this former model, the stretching of the crust induces the formation of melts at the base of the crust with the volume being dependent mostly on the stretching factor (β). According to our tests, a β value of approximately 1.5 or slightly larger would lead to realistic values for the thickness and density of the lower mass (7 km and 400 $\mathrm{kg/m^3}$) and would adequately fit the gravimetric observations. The stretching factor retrieved is a bit lower with respect to the estimate of Heine et al. (2013), who estimate a value of approximately 2.5 from basin analysis considerations. However, the authors warned that the method they use offers an upper bound for the β estimation and it would be representative for the stretching occurring in the upper crust, whereas our estimation would be mostly tied to the lower crust. Taking into account these considerations and the not-so-relevant differences between the stretching factors retrieved, we suggest that the rifting process occurred mostly uniformly throughout the crust.

According to McKenzie and Bickle (1988), such β values could lead to the formation of significant underplated melts that can eventually differentiate and migrate toward the surface. This way, we can more easily explain the high-frequency contribution of the gravity field that we observe in the lobster high.

The presence of such crustal intrusions could be an indication of a major melting episode affecting the asthenosphere and lithosphere. This could explain the change from marine to continental sedimentation in the second rift cycle of the Termit Basin, which could be due to the crustal doming induced by the impinging melts. The first rifting cycle of the WARS recorded marine sedimentation, which signalizes that the volcanism in the first postrift stage did not induce a doming. This could be compatible with the observation that the first volcanic postrift stage had a smaller duration of 8 Ma (96–88 Ma) compared to the volcanism of the second postrift phase that had a much longer duration from 23 Ma to the Quaternary.

The hypothesis of an existing magmatic body below the entire rift structures of the WARS related to the breakup of Gondwana in the Early Cretaceous is not so peculiar if we consider other similar locations worldwide. For example, along the West Siberian basin (Asia), the Permian flood basalts that cover the entire area produce linear positive anomalies in the gravity residuals (Vyssotski et al., 2006). Another example comes from the Amazon Basin, where the existence of an east–west rift system allowed the formation of broad intrusive magmatic bodies of Jurassic age. These intrusions cause positive linear trends in the Bouguer gravity anomaly field that follow the central areas of the basin (Milani and Filho, 2000; Bomfim et al., 2013). Finally, also along the Paranà Basin, in particular along the central part of that basin, the Bouguer gravity anomaly highs that separated the basin into two subareas were found. This northwest–southeast trend was discussed with the presence of extensive flood basalts of Cretaceous age (Fecher et al., 2017). It would be interesting to classify the rifts on a worldwide scale on the presence of volcanism and deep crustal densification, as a parameter useful for a rift classification, following the classification scheme defined by Ziegler and Cloetingh (2004).

CONCLUSION

A joint analysis of gravity and seismic reflection data has been carried out to estimate the depth of the basement below the northern rift basins of the WARS. From our results along the northern Termit rift basin, the gravity field obtained by using the existing sediment thickness model produces negative gravity values, which are also found in the residual gravity field. Here, the residual field is the outcome of the regression analysis between gravity and topography, which has the scope of reducing the gravity from the isostatic crustal thickness variations. On the contrary, in the southern areas around Lake Chad, there is no correspondence between the modeled effect of sediments and the residual gravity anomaly, leading to the conclusion that there is a hidden mass, which is compensating the gravity field of the sediments. Due to this fact, we hypothesize the existence of materials with high density (magmatic body) below the sediment layers that mostly cover the southern Termit and Ténére rift basins from Niger to the southern end of Lake Chad.

The high-density body is divided between the lower crust and the upper crust. The lower mass could be the expression of crustal thinning combined with underplating. We estimate a ratio of 1–7 between the thickness of the upper and lower masses from petrologic and petrophysical considerations.

We provide evidence that the integration of geophysical methods and petrophysical modeling is advantageous for the investigation of a long rift basin as WARS, and a multidisciplinary approach reveals greater insight into the structure. In our case, we retrieved an estimate of the stretching factor for the lower crust that, combined with independent estimates from other studies, suggests that the area was mostly uniformly stretched, affecting the whole crust during the rifting phase. This stretching is limited to the WARS, whereas the surrounding area of the Chad basin was unaffected and remained a shallow continental sag basin up to the present.

Our study demonstrates that GOCE satellite products, complemented with surface seismic exploration results, represent a fundamental support to investigate the deeper crustal structures.

ACKNOWLEDGMENTS

A Ph.D. grant to authors F. Maddaloni and T. Pivetta was provided by Regione Friuli Venezia Giulia (Italy) through a European Social Fund 50% cofunded fellowship. We acknowledge the BGI for the availability of terrestrial gravity data. F. Morsut and A. Pastorutti were involved in the early stages of the research. We thank an anonymous reviewer, reviewer B. J. Drenth, associate editor Y. Li, and the senior assistant editor J. T. Etgen for their thoughtful comments.

DATA AND MATERIALS AVAILABILITY

Data associated with this research are available and can be obtained by contacting the corresponding author.

APPENDIX A

EXPLORATION WELL LOCATIONS

The coordinates of the Chadina wells have been estimated from the available sources Genik (1993) and Zanguina et al. (1998). Table A-1 displays the locations of the exploration wells along the WARS areas of Niger and Chad.

Table A-1. Location of exploration wells along the WARS areas of Niger and Chad.

Country	Basins	Year	Well	Company	Age at terminal depth	Lithotype at terminal depth	Total depth (m)	Coordinates
Niger	Ténéré	1974/1975	Falchi-1	Texaco	Triassic-Permian	Continental siltstones	3740	10°57′15″E18°01′50″N
Niger	Grein/Kafra	1974/1975	Seguedine-1	Texaco	Precambrian	Gneiss, pegmatites	3144	10°57′15″E21°20′52″N
Niger	Grein/Kafra	1975	Tiffa-1	Texaco	Lower Cretaceous	Continental clastic	2782	11°15′21″E20°48′16″N
Niger	Termit	1975	Madama-1	Texaco	Santonian	Marine clastic	3810	12°38′35″E16°32′59″N
Niger	Termit	1975	Laguil-1	Exxon	Precambrian	Schists	2485	11°58′38″E16°04′58″N
Niger	Termit	1979	Yogou-1	Exxon	Coniacian	Marine shales	3995	13°43′35″E14°47′19″N
Niger	Termit	1980	Yogou-2	Exxon	Santonian	Marine shales	2728	13°44′59″E16°46′46″N
Niger	Termit	1979	Moul-1	Exxon	Santonian	Marine shales	3535	13°19′16″E15°05′27″N
Niger	Termit	1979/1980	Donga-1	Exxon	Albian	Continental sandstone	3201	12°13′37″E15°45′57″N
Niger	Termit	1980	Dilia-Langrin-1	Exxon	Precambrian	Granite	1988	11°54′31″E15°45′48″N
Niger	Termit	1982	Trakes-1	Elf	Santonian	Marine clastic	3659	13°24′34″E15°53′58″N
Niger	Termit	1982	Sokor-1	Elf	Maastrichtian	Continental sandstones	2470	12°55′20″E15°36′23″N
Niger	Termit	1982/1983	Sokor-2	Elf	Eocene	Continental clastic	1895	12°55′26″E15°33′53″N
Niger	Termit	1983	Sokor-3	Elf	Eocene	Continental clastic	1994	12°54′01″E15°40′07″N
Niger	Termit	1984	Sokor-4	Elf	Eocene	Continental clastic	1870	12°55′57″E15°34′46″N
Niger	Termit	1984	Sokor-5	Elf	Eocene	Continental clastic	1860	12°55′08″E15°36′19″N
Niger	Termit	1990	Goumeri-1	Elf	Paleocene	Continental sandstones	3280	12°34′23″E15°58′03″N
Niger	Termit	1990	Araga-1	Elf	Paleocene	Continental sandstones	2200	12°17′49″E16°47′23″N
Chad	Termit	1971	Kanem-1	Conoco	Coniacian	Marine shales	3726	*15°15′0″E14°43′0″N*
Chad	Termit	1971	Kosaki-1	Conoco	Albian/Aptian	Continental clastic	3314	*14°36′38″E14°12′36″N*
Chad	Termit	1975	Kanem-2	Conoco	Maastrichtian	Transitional sandstones	2169	*15°15′0″E14°43′0″N*
Chad	Termit	1975	Sedigi-1	Conoco	Cenomanian/Turonian	Marine clastic	3682	*14°16′60″E14°21′0″N*
Chad	Termit	1975	Largo-1	Conoco	Cenomanian	Marine clastic	3842	*14°10′60″E14°16′0″N*
Chad	Termit	1989	Sedigi-2	Conoco	Senonian	Marine shales and sandstones	3048	*15°15′0″E14°43′0″N*

REFERENCES

Abdelsalam, M. G., J.-P. Liégeois, and R. J. Stern, 2002, The Saharan Metacraton: Journal of African Earth Sciences, **34**, 119–136, doi: 10.1016/S0899-5362(02)00013-1.
Allen, P. A., and J. R. Allen, 2013, Basin analysis: Principles and application to petroleum play assessment, 3rd ed.: Wiley-Blackwell.
Amante, C., and B. W. Eakins, 2009, ETOPO1 1 arc-minute global relief model: Procedures, data sources and analysis: NOAA Technical Memorandum NESDIS NGDC-24, National Geophysical Data Center, NOAA, https://www.ngdc.noaa.gov/mgg/global/relief/ETOPO1/docs/ETOPO1.pdf, accessed 20 August 2021.
Barthelmes, F., 2013, Definition of functionals of the geopotential and their calculation from spherical harmonic models: Scientific Technical Report (STR), STR 09/02, 1–32.
Binks, R. M., and J. D. Fairhead, 1992, A plate tectonic setting for Mesozoic rifts of West and Central Africa: Tectonophysics, **213**, 141–151, doi: 10.1016/0040-1951(92)90255-5.
Blakely, R. J., 1995, Potential theory in gravity and magnetic applications, Transferred to digital print: University Press.
Bomfim, E. P., C. Braitenberg, and E. C. Molina, 2013, Mutual evaluation of global gravity models (EGM2008 and GOCE) and terrestrial data in Amazon Basin, Brazil: Geophysical Journal International, **195**, 870–882, doi: 10.1093/gji/ggt283.

Braitenberg, C., 2015, Exploration of tectonic structures with GOCE in Africa and across-continents: International Journal of Applied Earth Observation and Geoinformation, **35**, 88–95, doi: 10.1016/j.jag.2014.01.013.

Braitenberg, C., P. Mariani, and A. De Min, 2013, The European Alps and nearby orogenic belts sensed by GOCE: Bollettino Di Geofisica Teorica Ed Applicata, **54**, 321–334.

Braitenberg, C., P. Mariani, J. Ebbing, and M. Sprlak, 2011, The enigmatic Chad lineament revisited with global gravity and gravity-gradient fields: Geological Society, London, Special Publications 357, 329–341.

Braitenberg, C., and M. Zadro, 1999, Iterative 3D gravity inversion with integration of seismologic data: Bollettino Di Geofisica Teorica Ed Applicata, **40**, 469–475.

Braitenberg, C., M. Zadro, J. Fang, Y. Wang, and H. T. Hsu, 2000, The gravity and isostatic Moho undulations in Qinghai-Tibet plateau: Journal of Geodynamics, **30**, 489–505, doi: 10.1016/S0264-3707(00)00004-1.

Browne, S. E., and J. D. Fairhead, 1983, Gravity study of the Central African rift system: A model of continental disruption 1. The Ngaoundere and Abu Gabra Rifts: Tectonophysics, **94**, 187–203, doi: 10.1016/0040-1951(83)90016-1.

Bureau Gravimetrique International (BGI), 2016, http://bgi.obs-mip.fr/data-products/gravity-databases/land-gravity-data/, doi: 10.18168/BGI, accessed 20 August 2021.

Burke, K., 1976, The Chad Basin: An active intra-continntal basin, *in* M. H. P. Bott, ed., Developments in geotectonics: Elsevier 12, 197–206.

Commission of the Geological Map of the World/UNESCO, 1990, International geological map of Africa at 1:5000000, CGMW/UNESCO Paris.

Crenn, Y., 1955, Anomalies de la pesanteur au Tchad: Complément aux rapports de R. Godivier et Y. Crenn, report of Office de la recherche scientifique et technique outre-mer (ORSTOM), p. 41.

Dorbath, C., L. Dorbath, J. D. Fairhead, and G. W. Stuart, 1986, A teleseismic delay time study across the Central African shear zone in the Adamawa region of Cameroon, West Africa: Geophysical Journal International, **86**, 751–766, doi: 10.1111/j.1365-246X.1986.tb00658.x.

Eshagh, M., and M. Pitoňák, 2019, Elastic thickness determination from on-orbit GOCE data and CRUST1.0: Pure and Applied Geophysics, **176**, 685–696, doi: 10.1007/s00024-018-2018-3.

Eyike, A., and J. Ebbing, 2015, Lithospheric structure of the West and Central African rift system from regional three-dimensional gravity modelling: South African Journal of Geology, **118**, 285–298, doi: 10.2113/gssajg.118.3.285.

Eyike, A., S. C. Werner, J. Ebbing, and E. M. Dicoum, 2010, On the use of global potential field models for regional interpretation of the West and Central African rift system: Tectonophysics, **492**, 25–39, doi: 10.1016/j.tecto.2010.04.026.

Fairhead, J. D., 1986, Geophysical controls on sedimentation within the African Rift Systems: Geological Society, London, Special Publications 25, 19–27.

Fairhead, J. D., and C. M. Green, 1989, Controls on rifting in Africa and the regional tectonic model for the Nigeria and East Niger rift basins: Journal of African Earth Sciences (and the Middle East), **8**, 231–249, doi: 10.1016/S0899-5362(89)80027-2.

Fairhead, J. D., C. M. Green, S. M. Masterton, and R. Guiraud, 2013, The role that plate tectonics, inferred stress changes and stratigraphic unconformities have on the evolution of the West and Central African rift system and the Atlantic continental margins: Tectonophysics, **594**, 118–127, doi: 10.1016/j.tecto.2013.03.021.

Fairhead, J. D., and C. S. Okereke, 1987, A regional gravity study of the West African rift system in Nigeria and Cameroon and its tectonic interpretation: Tectonophysics, **143**, 141–159, doi: 10.1016/0040-1951(87)90084-9.

Faure, H., 1962, Reconnaissance géologique des formations sédimentaires postpaléozoiques du Niger oriental: Edité par le Bureau de recherches géologiques et minières avec le concours du'Fonds d'aide et de coopération'et du Ministèrede l'éducation nationale et publié par la Direction des mines et de la géologiede la République de Niger.

Fecher, T., R. Pail, and T. Gruber, , The GOCO Consortium, University of Bonn, Institute of Geodesy and Geoinformation, Schuh, W.-D., J. Kusche, J. M. Brockmann, I. Loth, S. Müller, A. Eicker, and J. Schall, , Graz University of Technology, Institute of Geodesy, Mayer-Gürr, T., A. Kvas, B. Klinger, D. Rieser, and N. Zehentner, , Austrian Academy of Sciences, Space Research Institute, Baur, O., E. Höck, and S. Krauss, , University of Bern, Astronomical Institute, Jäggi, A., U. Meyer, L. Prange, and A. Maier, 2017, GOCO05c: A new combined gravity field model based on full normal equations and regionally varying weighting: Surveys in Geophysics, **38**, 571–590.

Fleitout, L., C. Froidevaux, and D. Yuen, 1986, Active lithospheric thinning: Tectonophysics, **132**, 271–278, doi: 10.1016/0040-1951(86)90037-5.

Förste, C., S. Bruinsma, O. Abrikosov, F. Flechtner, J.-C. Marty, J.-M. Lemoine, C. Dahle, H. Neumayer, F. Barthelmes, R. König, and R. Biancale, 2014, EIGEN-6C4 — The latest combined global gravity field model including GOCE data up to degree and order 1949 of GFZ Potsdam and GRGS Toulouse: EGU General Assembly Conference Abstracts, 16.

Fountain, D. M., and M. H. Salisbury, 1981, Exposed cross-sections through the continental crust: Implications for crustal structure, petrology, and evolution: Earth and Planetary Science Letters, **56**, 263–277, doi: 10.1016/0012-821X(81)90133-3.

Genik, G. J., 1992, Regional framework, structural and petroleum aspects of rift basins in Niger, Chad and the Central African Republic (C.A.R.): Tectonophysics, **213**, 169–185, doi: 10.1016/0040-1951(92)90257-7.

Genik, G. J., 1993, Petroleum geology of Cretaceous-Tertiary rift basins in Niger, Chad, and Central African Republic: AAPG Bulletin, **77**, 1405–1434.

Gibb, R. A., and M. D. Thomas, 1976, Gravity signature of fossil plate boundaries in the Canadian Shield: Nature, **262**, 199–200, doi: 10.1038/262199a0.

Guiraud, R., and R. M. Binks, 1992, Chronology and geodynamic setting of Cretaceous-Cenozoic rifting in West and Central Africa: Tectonophysics, **213**, 227–234, doi: 10.1016/0040-1951(92)90260-D.

Guiraud, R., and W. Bosworth, 1997, Senonian basin inversion and rejuvenation of rifting in Africa and Arabia: Synthesis and implications to plate-scale tectonics: Tectonophysics, **282**, 39–82, doi: 10.1016/S0040-1951(97)00212-6.

Guiraud, R., W. Bosworth, J. Thierry, and A. Delplanque, 2005, Phanerozoic geological evolution of Northern and Central Africa: An overview: Journal of African Earth Sciences, **43**, 83–143, doi: 10.1016/j.jafrearsci.2005.07.017.

Guiraud, R., and J.-C. Maurin, 1992, Early cretaceous rifts of Western and Central Africa: An overview: Tectonophysics, **213**, 153–168, doi: 10.1016/0040-1951(92)90256-6.

Harouna, M., and R. P. Philp, 2012, Potential petroleum source rocks in the Termit Basin, Niger: Journal of Petroleum Geology, **35**, 165–185, doi: 10.1111/j.1747-5457.2012.00524.x.

Heine, C., J. Zoethout, and R. D. Müller, 2013, Kinematics of the South Atlantic rift: Solid Earth, **4**, 215–253, doi: 10.5194/se-4-215-2013.

Ince, E. S., F. Barthelmes, S. Reißland, K. Elger, C. Förste, F. Flechtner, and H. Schuh, 2019, ICGEM – 15 years of successful collection and distribution of global gravitational models, associated services and future plans: Earth System Science Data, **11**, 647–674, doi: 10.5194/essd-11-647-2019.

Kirby, J. F., 2014, Estimation of the effective elastic thickness of the lithosphere using inverse spectral methods: The state of the art: Tectonophysics, **631**, 87–116, doi: 10.1016/j.tecto.2014.04.021.

Lagrula, M. J., 1952, Rapport de reconnaissance gravimétrique au territoire du Tchad: report of Office de la recherche scientifique et technique outremer (ORSTOM), p. 24.

Liang, Q., C. Chen, and Y. Li, 2014, 3-D inversion of gravity data in spherical coordinates with application to the GRAIL data: Journal of Geophysical Research: Planets, **119**, 1359–1373.

Louis, P., 1970, Contribution géophysique à la connaissance géologique du bassin du lac Tchad, 355.

McKenzie, D., and M. J. Bickle, 1988, The volume and composition of melt generated by extension of the lithosphere: Journal of Petrology, **29**, 625–679, doi: 10.1093/petrology/29.3.625.

Milani, E. J., and A. T. Filho, 2000, Sedimentary basins of South America, in Cordani, U. G., E. J. Milani, A. T. Filho, and D. A. Campos, eds., 31st International Geologic Congress, Tectonic evolution of South America: Rio de Janeiro, 389–449.

Moussa, A., I. Moussa, H. Abderamane, M. Schuste, H.T. Mackaye, A. Likius, D. Ahounta, P. Duringer, and P. Vignaud, 2013, Synthèse géologique des dépôts sédimentaires continentaux d'âge Miocène et Pliocène du bassin du Tchad: Proposition de nouvelles coupes géologiques à travers le bassin: Revue scientifique du Tchad, 22–23.

Olabode, S. O., J. A. Adekoya, and P. S. Ola, 2015, Distribution of sedimentary formations in the Bornu Basin, Nigeria: Petroleum Exploration and Development, **42**, 674–682, doi: 10.1016/S1876-3804(15)30062-8.

Oldenburg, D. W., 1974, The inversion and interpretation of gravity anomalies: Geophysics, **39**, 526–536, doi: 10.1190/1.1440444.

Parker, R. L., 1973, The rapid calculation of potential anomalies: Geophysical Journal International, **31**, 447–455, doi: 10.1111/j.1365-246X.1973.tb06513.x.

Pavlis, N. K., S. A. Holmes, S. C. Kenyon, and J. K. Factor, 2012, The development and evaluation of the Earth Gravitational Model 2008 (EGM2008): Journal of Geophysical Research: Solid Earth, **117**, B04406, doi: 10.1029/2011JB008916.

Pivetta, T., and C. Braitenberg, 2020, Sensitivity of gravity and topography regressions to earth and planetary structures: Tectonophysics, **774**, 228299, doi: 10.1016/j.tecto.2019.228299.

Plomerová, J., V. Babuška, C. Dorbath, L. Dorbath, and R. J. Lillie, 1993, Deep lithospheric structure across the Central African shear zone in Cameroon: Geophysical Journal International, **115**, 381–390, doi: 10.1111/j.1365-246X.1993.tb01193.x.

Pouclet, A., and J. P. Karche, 1988, Petrology and geochemistry of the Cenozoic volcanism in Eastern Niger (West Africa), in Mesozoic to present-day magmatism of the African Plate and its structural setting: International Center for Training and Exchanges in the Geosciences, 1988/15, 194–195.

Shellnutt, J. G., N. H. T. Pham, S. W. Denyszyn, M.-W. Yeh, and T.-Y. Lee, 2017, Timing of collisional and post-collisional Pan-African Orogeny silicic magmatism in south-central Chad: Precambrian Research, **301**, 113–123, doi: 10.1016/j.precamres.2017.08.021.

Stuart, G. W., J. D. Fairhead, L. Dorbath, and C. Dorbath, 1985, A seismic refraction study of the crustal structure associated with the Adamawa Plateau and Garoua Rift, Cameroon, West Africa: Geophysical Journal International, **81**, 1–12, doi: 10.1111/j.1365-246X.1985.tb01346.x.

Suleiman, A. A., C. Magee, C. A.-L. Jackson, and A. J. Fraser, 2017, Igneous activity in the Bornu Basin, onshore NE Nigeria; implications for opening of the South Atlantic: Journal of the Geological Society, **174**, 667–678, doi: 10.1144/jgs2016-107.

Torge, W., and J. Müller, 2012, Geodesy, 4th ed.: De Gruyter.

Uieda, L., V. C. F. Barbosa, and C. Braitenberg, 2016, Tesseroids: Forward-modeling gravitational fields in spherical coordinates: Geophysics, **81**, no. 5, F41–F48, doi: 10.1190/geo2015-0204.1.

United Nations Environment Porgramme, 2004, Lake Chad Basin, in Fortnam, M. P. and J. A. Oguntola, eds., Global International Waters Assessment (GIWA) regional assessment 43.

Vidigal-Souza, P. A., D. B. Vilas-Boas, A. G. Brandao, and M. Holz, 2020, Seismic stratigraphy of Camamu Basin, Northeastern Brazil: Pure and Applied Geophysics, **177**, 5207–5224, doi: 10.1007/s00024-020-02580-3.

Vyssotski, A. V., V. N. Vyssotski, and A. A. Nezhdanov, 2006, Evolution of the West Siberian Basin: Marine and Petroleum Geology, **23**, 93–126, doi: 10.1016/j.marpetgeo.2005.03.002.

Wan, L., J. Liu, F. Mao, M. Lv, and B. Liu, 2014, The petroleum geochemistry of the Termit Basin, Eastern Niger: Marine and Petroleum Geology, **51**, 167–183, doi: 10.1016/j.marpetgeo.2013.11.006.

Watts, A. B., 2001, Isostasy and flexure of the lithosphere: Cambridge University Press.

Wennekers, J. H. N., F. K. Wallace, and Y. I. Abugares, 1996, The geology and hydrocarbons of the Sirt Basin: Proceedings of the First Symposium on the Sedimentary Basins of Libya, Tripoli, **III**, Elsevier Publishers, 1–56.

Wilson, M., and R. Guiraud, 1992, Magmatism and rifting in Western and Central Africa, from Late Jurassic to Recent times: Tectonophysics, **213**, 203–225, doi: 10.1016/0040-1951(92)90259-9.

Wilson, M., R. Guiraud, C. Moreau, and Y.-C. Bellion, 1998, Late Permian to recent magmatic activity on the African-Arabian margin of Tethys: Geological Society, London, Special Publications 132, 231–263,.

Zanguina, M., A. Bruneton, and R. Gonnard, 1998, An introduction to the petroleum potential of Niger: Journal of Petroleum Geology, **21**, 83–103, doi: 10.1111/j.1747-5457.1998.tb00647.x.

Ziegler, P. A., and S. Cloetingh, 2004, Dynamic processes controlling evolution of rifted basins: Earth-Science Reviews, **64**, 1–50, doi: 10.1016/S0012-8252(03)00041-2.

1. Francesca Maddaloni, Carla Braitenberg, Mikhail K. Kaban, Magdala Tesauro, Damien Delvaux. 2021. The Congo Basin: Subsurface structure interpreted using potential field data and constrained by seismic data. *Global and Planetary Change* **205**, 103611. [Crossref]